Nature Communications

https://doi.org/10.1038/s41467-026-73383-8

Article in Press

IRAK2 deficiency causes immune dysregulation through defective Myddosome assembly and enhanced interferon responses

Received: 5 September 2025

Accepted: 11 May 2026

Cite this article as: Fei, Y., Liu, L., Ma, S. *et al.* IRAK2 deficiency causes immune dysregulation through defective Myddosome assembly and enhanced interferon responses. *Nat Commun* (2026). https://doi.org/10.1038/s41467-026-73383-8

Yudie Fei, Lin Liu, Shuangyue Ma, Ying Jin, Shihao Wang, Liang Zhang, Jun Yang, Yi Liu, Meiping Lu, Jing Xue, Jingyi Li, Xiang Chen, Jun Wang, Yuhao Yao, Chenlu Liu, Jiahui Zhang, Xu Han, Jinjian Fu, Zhijuan Kang, Yusha Wang, Xiangwei Sun, Changming Zhang, Tingyan He, Zhihui Liu, Li Guo, Chengshun Chen, Hongmei Zhao, Xingjian Gao, Hua Zhong, Lihong Wen, Xiaomin Yu, Zhihong Liu & Qing Zhou

IRAK2 deficiency causes immune dysregulation through defective Myddosome assembly and enhanced interferon responses

Yudie Fei[1, 2, #], Lin Liu[3, 4, #], Shuangyue Ma[1, #], Ying Jin[5, #], Shihao Wang[1, 6, #], Liang Zhang[7, 8, 9, 10, #], Jun Yang[11, #], Yi Liu[12, #], Meiping Lu[13, #], Jing Xue[14, #], Jingyi Li[15, #], Xiang Chen[1, #], Jun Wang[1, 16, #], Yuhao Yao[4, #], Chenlu Liu[4, #], Jiahui Zhang[2, #], Xu Han[1, 16, 17, #], Jinjian Fu[4, #], Zhijuan Kang[7, 8, 9, 10, #], Yusha Wang[1, 16], Xiangwei Sun[1], Changming Zhang[2], Tingyan He[11], Zhihui Liu[12], Li Guo[13], Chengshun Chen[15], Hongmei Zhao[18], Xingjian Gao[2], Hua Zhong[14], Lihong Wen[14], Xiaomin Yu[1, 14, *, +], Zhihong Liu[5, 1, *, +], Qing Zhou[1, 4, 16, 19, *, +]

1 Liangzhu Laboratory, Zhejiang University, Hangzhou, China

2 National Clinical Research Center for Kidney Diseases, Jinling Hospital, Affiliated Hospital of Medical School, Nanjing University, Nanjing, China

3 Urology & Nephrology Center, Department of Nephrology, Zhejiang Provincial People's Hospital (Affiliated People's Hospital, Hangzhou Medical College), Hangzhou, China

4 Life Sciences Institute, Zhejiang University, Hangzhou, China

5 National Clinical Research Center of Kidney Diseases, Jinling Clinical Medical College, Nanjing Medical University, Nanjing, China

6 Cell and Molecular Biology Laboratory, Affiliated Zhoushan Hospital of Wenzhou Medical University, Zhoushan, China

7 The Affiliated Children's Hospital of Xiangya School of Medicine, Central South University (Hunan Children's Hospital), Changsha, Hunan, China

8 Department of Nephrology, Rheumatology and Immunology, Hunan Children's Hospital, Changsha, Hunan, China

9 The School of Pediatrics, Hengyang Medical School, University of South China, Hengyang 421001, Hunan, China

10 Hunan Provincial Key Laboratory of Pediatric Orthopedics, Changsha, Hunan, China

11 Department of Rheumatology and Immunology, Shenzhen Children's Hospital, Shenzhen, China

12 Department of Rheumatology and Immunology, West China Hospital, Sichuan University, Chengdu, China

13 Department of Rheumatology Immunology and Allergy, Children's Hospital, Zhejiang University School of Medicine, Hangzhou, China

14 Department of Rheumatology, The Second Affiliated Hospital, Zhejiang University School of Medicine, Hangzhou, Zhejiang, China

15 Department of Rheumatology and Immunology, The First Hospital Affiliated to The Army Medical University (Third Military Medical University), Chongqing, China

16 Department of Rheumatology, Sir Run Run Shaw Hospital, Zhejiang University School of Medicine, Hangzhou, China

17 Hangzhou Institute of Medicine, Chinese Academy of Sciences, Hangzhou, China

18 Department of Digestive Nutrition, Hunan Children's Hospital, Changsha, China

19 State Key Laboratory of Common Mechanism Research for Major Diseases, Institute of Basic Medical Sciences & School of Basic Medicine, Chinese Academy of Medical Sciences & Peking Union Medical College, Beijing, China

#These authors contributed equally: Yudie Fei, Lin Liu, Shuangyue Ma, Ying Jin, Shihao Wang, Liang Zhang, Jun Yang, Yi Liu, Meiping Lu, Jing Xue, Jingyi Li, Xiang Chen, Jun Wang, Yuhao Yao, Chenlu Liu, Jiahui Zhang, Xu Han, Jinjian Fu, Zhijuan Kang.

*These authors jointly supervised this work: Qing Zhou, Zhihong Liu, Xiaomin Yu.

+Corresponding authors: zhouqingnwu@gmail.com; liuzhihong@zju.edu.cn; yuxiaomin@zju.edu.cn.

Abstract

Interleukin-1 receptor-associated kinase 2 (IRAK2) is essential for the Myddosome complex formation downstream of Toll-like receptors. We identify twelve patients with a homozygous loss-of-function copy number variant in *IRAK2*, designated *IRAK2-Δex2*. Most patients present with recurrent infections, autoantibody production, and gastrointestinal ulceration. Two patients were clinically diagnosed with primary immunodeficiency, while the majority fulfill diagnostic criteria for autoimmune or autoinflammatory diseases. The IRAK2-Δex2 protein fails to interact with IRAK4, leading to impaired activation of nuclear factor kappa B signaling via the Myddosome complex. An elevated type I interferon signature is observed in the patients, which is confirmed in bone marrow-derived macrophages from knock-in mice and knockout cell lines. Mechanistically, our data are consistent with engagement of a TRIF-dependent interferon pathway. Baricitinib attenuates the elevated interferon signature in patient-derived cells *ex vivo* and cell lines. Here, we show IRAK2 deficiency as a monogenic immune dysregulation disorder.

Introduction

Toll-like receptor (TLR) signaling pathways are classic pattern recognition receptors that play an essential role in immune defense and in mediating cross-talk between the innate and adaptive immune systems[1]. Upon ligand recognition, myeloid differentiation factor 88 (MyD88), interleukin-1 receptor-associated kinase 4 (IRAK4), and interleukin-1 receptor-associated kinase 2 (IRAK2) are recruited to the membrane to form the Myddosome complex[2], which primarily activates the nuclear factor kappa B (NF-κB) and mitogen-activated protein kinase (MAPK) signaling pathways[1].

IRAK2 consists of a death domain (DD), a proline, serine, and threonine-rich linker, a kinase domain, and a C-terminal domain. Exon 2 encodes part of the DD, which is essential for Myddosome assembly[2]. IRAK1 and IRAK2 sequentially regulate TLR signaling[3]. IRAK2 is indispensable for the persistence of cytokine gene transcription and NF-κB activation downstream of all TLRs except TLR3[4]. Consistent with its role, *Irak2* knockout (KO) mice are resistant to shock responses induced by LPS and CpG DNA[3].

In this work, we identify twelve patients harboring a homozygous loss-of-function (LoF) copy number variant (CNV) in *IRAK2*, designated *IRAK2*-Δ*ex2*. The *IRAK2*-Δ*ex2* mutation impairs Myddosome-dependent signal transduction by disrupting its interaction with IRAK4. Consistently, impaired NF-κB activation in knock-in mice is associated with blunted inflammatory responses to endotoxin, resulting in reduced immunopathology but compromised bacterial clearance. In addition, an elevated type I interferon (IFN) signature is observed in some of the patients, mice, and THP-1 cell lines carrying the mutation. Our data are supportive of an amplified TRIF-dependent pathway for IFN signaling, with secondary modulation by NF-κB/MAPK pathways. Collectively, our work provides genetic and mechanistic evidence for an immune dysregulation disorder, which we term DIRAK2 (Deficiency of IRAK2).

Results

Mutation in *IRAK2* defines an immune dysregulation disorder

We initially identified a homozygous CNV in the *IRAK2* gene by whole exome sequencing (WES) in two patients presenting with immune dysregulation disorders. Subsequently, we identified additional ten patients, resulting in a total of twelve patients from eleven unrelated, non-consanguineous Chinese families (Fig. 1a). Notably, two patients (P1 and P2) experienced recurrent pulmonary infections (Fig. 1b, c) and were diagnosed with primary immunodeficiencies (PIDs). All heterozygous carriers were unaffected. Both male and female individuals carrying the homozygous mutation were affected. Among the 12 patients, 11 were clinically affected and only one (P4) was preclinical, suggesting possible reduced penetrance. Age at onset was variable, ranging from 1 month of age to adulthood.

Among the twelve patients, six (50%) experienced recurrent infections requiring hospitalization (Supplementary Table 1). The pathogens included Gram-positive and negative bacteria, fungi, and viruses (Supplementary Table 2). Notably, P2 died at the age of 65 years due to severe pneumonia and macrophage activation syndrome. Six (50%) patients tested positive for autoantibodies (Supplementary Table 3). Among them, four were diagnosed with systemic lupus erythematosus (SLE) accompanied by lupus nephritis (P3, P5, P6, and P7; Fig. 1d-f and Supplementary Fig. 1a, b), one with Hashimoto's thyroiditis (P11), and one exhibited a progressively elevated type I IFN signature alongside rising antinuclear antibody (ANA) titers (Supplementary Fig. 1c). Two patients primarily exhibited gastrointestinal (GI) involvement, including abdominal pain, vomiting, and bloody stools. Gastrointestinal endoscopy revealed multiple ulcers throughout the digestive tract (Fig. 1g and Supplementary Fig. 1d), and histopathology showed active or chronic inflammation, cryptitis, and crypt abscesses in the ileocecal region (Fig. 1h and Supplementary Fig. 1e). P10 was diagnosed with juvenile idiopathic

arthritis (JIA), presenting with pain and restricted mobility in the left knee and hips (Fig. 1i). P12 was diagnosed with autoimmune encephalitis (Supplementary Fig. 1f). The clinical phenotypic spectrum among the twelve patients is broad. Based on predominant manifestations and clinical diagnosis, patients can be categorized into three phenotypic subgroups: immunodeficiency-predominant (P1 and P2), autoimmunity-predominant (P3-7, P11, and P12), and autoinflammation-predominant (P8-10). A summary of the clinical manifestations across all twelve patients, highlighting the frequency and distribution of key phenotypes, is provided in Fig. 1j.

P1 and P2 were treated with antibiotics and intravenous immunoglobulin (IVIG) for recurrent infections. The majority of patients received immunosuppressive therapy, including glucocorticoids (P3, P5-10), hydroxychloroquine (HCQ) (P3, P5, and P6), cyclophosphamide (CTX) (P3 and P9), tacrolimus or sirolimus (P3, P5, and P7), mycophenolate mofetil (MMF) or azathioprine (AZA) (P3, P5, P6, P8, and P9), belimumab or telitacicept (P3, P5, and P6), infliximab (P8) and methotrexate (MTX) (P10) (Supplementary Table 1). Detailed clinical histories are provided in the Supplementary Patient Information section of the Supplementary Information.

WES or whole genome sequencing (WGS) identified a homozygous CNV in the *IRAK2* gene (Supplementary Fig. 2a, b). We further confirmed that all twelve patients shared the same genomic breakpoints (NC_000003.12: g.10176864_10180995delinsTGGA, NM_001570.4: c.95_277del, p.Ala32_Trp93delinsGly) (Fig. 1k). No other rare variants of uncertain significance or CNVs in genes previously associated with immune disorders were detected in these patients. The CNV resulted in an in-frame deletion of exon 2 (Supplementary Fig. 2c), designated *IRAK2-*Δ*ex2*. The truncated transcripts were still transcribed at a comparable level to the wild-type (WT) transcripts in both humans and mice (Fig. 1l, m and Supplementary Fig. 2d-f). Aside from one frameshift variant (p.Q68AfsTer31), homozygous alleles in gnomAD v4.1.0 with a CADD_phred score above 25 retained the ability to activate NF-κB signaling (Supplementary Fig. 2g), further

supporting the rarity of homozygous LoF variants in *IRAK2*. Previously reported single nucleotide variants (SNVs), including p.L78P and p.R506W[5], also preserved NF-κB-activating capacity (Supplementary Fig. 2g).

Disrupted interaction between IRAK2-Δex2 and IRAK4

Based on the structure of the Myddosome complex[2], the deleted region of IRAK2 is located at the interaction surface with IRAK4 (Fig. 2a). Interface analysis estimated an IRAK2-IRAK4 buried surface area (BSA) of ~578 Å² per interface side for the full-length complex, with the deleted segment (A32-W93) contributing ~552 Å². In HEK293T-*IRAK2* KO cells, the mutation disrupted the interaction between IRAK2 and IRAK4, but with no significant change in its interaction with tumor necrosis factor receptor-associated factor 6 (TRAF6) (Fig. 2b and Supplementary Fig. 3a).

IRAK2-Δex2 disrupts signal transduction via Myddosome

The direct interaction between IRAK2 and IRAK4 is critical for signal transduction of most TLRs except TLR3[4]. IRAK2-Δex2 failed to activate NF-κB and MAPK signaling compared with IRAK2-WT in HEK293T-TLR4 stable cell lines (Fig. 2c), phenocopying the impairment observed in *IRAK2* KO cells (Supplementary Fig. 3b-d). We next examined cytokine production by peripheral blood mononuclear cells (PBMCs) from patients in response to LPS (TLR4 agonist) or R848 (TLR7/8 agonist). Both the mRNA (Fig. 2d and Supplementary Fig. 3e) and protein levels (Fig. 2e and Supplementary Fig. 3f) of cytokines downstream of the NF-κB signaling pathway, including IL-1β, IL-6 and IL-10, showed reduced induction following LPS or R848 stimulation in patients' PBMCs compared with unaffected controls. MAPK pathway activation was also impaired, although the defect was less pronounced than that observed for NF-κB (Supplementary Fig. 3g, h). To study cell-type-specific immune signatures, cytometry by time of flight (CyTOF) and single-cell RNA sequencing (scRNA-seq) were performed on PBMCs from patients (P3 and P4) and controls.

There were no significant changes in the composition of PBMCs with or without LPS stimulation (Supplementary Fig. 4a-c). Cytokine secretion defects were most pronounced in monocytes and dendritic cells (DCs) from patients following LPS stimulation (Fig. 2f). Consistent with CyTOF findings, scRNA-seq also revealed impaired NF-κB signaling in monocytes and pDCs after LPS stimulation (Fig. 2g and Supplementary Fig. 4d), highlighting the critical role of IRAK2 in regulating these immune cells.

Impaired inflammatory response in *Irak2*$^{\Delta ex2/\Delta ex2}$ mice

To further explore the physiological function of the *Irak2*-Δ*ex2* mutation *in vivo*, we generated homozygous knock-in *Irak2*$^{\Delta ex2/\Delta ex2}$ mice. *Irak2*$^{\Delta ex2/\Delta ex2}$ mice exhibited higher survival rate at 7 days post-intraperitoneal injection with high-dose LPS (Fig. 3a), consistent with the reports in *Irak2* KO mice[3,6]. Serum cytokine and chemokine levels were significantly reduced in *Irak2*$^{\Delta ex2/\Delta ex2}$ mice compared with WT mice, while no differences were observed at baseline (Fig. 3b). *Il1b* and *Il6* expression levels in the kidney, liver, and spleen were markedly lower in the *Irak2*$^{\Delta ex2/\Delta ex2}$ group following LPS stimulation (Fig. 3c and Supplementary Fig. 5a). Notably, hematoxylin and eosin (H&E) staining of liver tissue showed less severe LPS-induced acute liver injury[7] in *Irak2*$^{\Delta ex2/\Delta ex2}$ mice (Fig. 3d), consistent with lower proinflammatory cytokine levels. In an intraperitoneal *E. coli* infection model, *Irak2*$^{\Delta ex2/\Delta ex2}$ mice exhibited impaired bacterial clearance (Fig. 3e), accompanied by reduced induction of inflammatory cytokines in the peripheral blood (Fig. 3f and Supplementary Fig. 5b). Collectively, these findings indicate that the *Irak2*-Δ*ex2* mutation dampens inflammatory cytokine responses to acute endotoxin and bacterial challenge, potentially reducing LPS-induced immunopathology while increasing susceptibility to infection due to impaired pathogen clearance.

We evaluated 50-week-old mice for body weight, spleen index, autoantibody profiles, serum cytokines, tissue inflammation, and kidney histology. No significant differences were observed between mutant mice and WT littermates (Supplementary Fig. 5c-l). Notably, while humans

express a single *IRAK2* transcript, mice express four *Irak2* isoforms, two of which naturally lack exon2[8]. This species-specific isoform context may attenuate the functional impact of the mutation in mice and, together with the specific pathogen-free (SPF) environment, may underlie the absence of spontaneous pathology in mice.

Bone marrow-derived macrophages (BMDMs) from *Irak2*$^{\Delta ex2/\Delta ex2}$ mice showed defects in multiple Tlr pathways, including Tlr4, Tlr7/8, Tlr2/Tlr6, Tlr1/Tlr2, and Tlr9 (Fig. 3g, h and Supplementary Fig. 6a, b), following stimulations with their agonist LPS, R848, FSL-1, Pam_3Cys-Ser-$(Lys)_4$ (PAM3), and ODN2006, respectively. Tlr3 signaling remained intact upon poly(I:C) stimulation (Supplementary Fig. 6c). These findings indicate that the mutation causes broad Myddosome-mediated signaling impairment.

Elevated type I interferon activity in DIRAK2 patients

Serum IFN-β levels were significantly higher in patients (P1, P3, P4, P8, P9, and P11) compared with unaffected controls (Fig. 4a), and the baseline phosphorylated IRF3 levels were markedly elevated in P1, P8, and P11 (Fig. 4b and Supplementary Fig. 7a). Expansion of $CD8^+$ T cells[9] (Supplementary Fig. 4a-c) and aberrant inflammatory responses (Supplementary Fig. 7b) were also noted in patients. Gene set enrichment analysis (GSEA) revealed upregulation of interferon α and interferon γ responses in patients' PBMCs following LPS stimulation (Fig. 4c). Specific genes in the type I IFN pathway were significantly upregulated in inflammatory monocytes from the patients following LPS stimulation (Fig. 4d-f and Supplementary Fig. 8 and Supplementary Fig. 9). This was recapitulated in both BMDMs from *Irak2*$^{\Delta ex2/\Delta ex2}$ mice and Phorbol 12-myristate 13-acetate (PMA)-differentiated THP-1 KO cells (Fig. 4g, h and Supplementary Fig. 10a-c).

To better delineate DIRAK2, we performed comparative analyses with monogenic disorders affecting the TLR-Myddosome pathway (Supplementary Table 4) and with type I

interferonopathies (Fig. 4i). TLR4 deficiency was associated with impaired LPS responsiveness and GI bacterial infections[10]. Deficiencies of core Myddosome components disrupted signaling downstream of multiple TLRs and resulted in susceptibility to multiple pathogens. Notably, infections in the DIRAK2 cohort were generally less severe than those reported in MyD88 or IRAK4 deficiencies. Several DIRAK2 patients exhibited an elevated type I IFN signature, a feature not explicitly described in MyD88 or IRAK4 deficiencies. Principal component analysis (PCA) based on IFN-related genes clustered DIRAK2 samples with autoimmunity/autoinflammation close to interferonopathies (Fig. 4i). Given that IRAK2 acts downstream of MyD88 and IRAK4 and has redundant functions with IRAK1, we speculated that DIRAK2 may lead to an imbalance or rerouting of the downstream signaling rather than a complete blockade.

Supportive evidence for TRIF-TBK1/IKKε involvement in IFN responses, with secondary NF-κB/MAPK input

To further establish the connection between IRAK2 and type I IFN signaling, we reconstituted *IRAK2* KO THP-1 cells with IRAK2-WT and IRAK2-Δex2, using empty vector (EV) as control. Cells expressing IRAK2-WT exhibited reduced IFN signaling compared with EV and IRAK2-Δex2 (Fig. 5a, b). Inhibitors of TIRAP or TRIF effectively suppressed the aberrant IFN response (Fig. 5c, d), and genetic TRIF knockdown yielded concordant results (Fig. 5e, f and Supplementary Fig. 10d), suggesting that the increased IFN response is TRIF-dependent. Downstream, inhibition of TBK1/IKKε effectively reduced the IFN signaling (Fig. 5g, h). TAK1 inhibition partially attenuated the IFN response (Fig. 5g, h), suggesting a secondary, modulatory contribution of NF-κB and MAPK pathways. In parallel, NF-κB-dependent negative regulators, including *IL10* (IL-10) and *TNFAIP3* (A20), which have been reported to negatively regulate IFN signaling[11-13], showed blunted induction following the LPS stimulation in the absence of functional IRAK2 (Supplementary Fig. 6c and Supplementary Fig. 10e). Together, these findings suggest a model

in which type I IFN signaling is amplified through the TRIF-dependent axis, with secondary modulation contributed by NF-κB and MAPK pathways.

As several patients presented with autoimmune manifestations, we evaluated the effect of Baricitinib (a Janus kinase inhibitor) on type I IFN signaling in PBMCs *ex vivo* and PMA-differentiated THP-1 cell lines. PBMCs from two patients (P4 and P11), both of whom had not received any treatment, exhibited progressively elevated type I IFN signature that were attenuated following Baricitinib treatment (Fig. 5i and Supplementary Fig. 10f). Baricitinib also effectively downregulated type I IFN signaling in the PMA-differentiated *IRAK2* KO THP-1 cell lines (Fig. 5j, k). These findings suggest that IFN-pathway-targeted approaches may be a potential therapeutic option for DIRAK2 patients with autoimmune manifestations. However, further mechanistic studies and clinical evaluations are necessary to determine safety and efficacy.

Discussion

We identified a homozygous LoF CNV, *IRAK2-Δex2*, in twelve patients. This mutation results in the deletion of the entire exon 2 along with portions of the flanking intronic regions. Notably, this genomic region is a recognized hotspot for *Alu*-mediated homologous recombination[14], providing a plausible mechanism for the mutation. The *IRAK2-Δex2* mutation is recorded in gnomAD SVs v4.1.0 with a total population frequency of 0.0005631. Notably, the *IRAK2-Δex2* mutation is more prevalent in the East Asian population, with a frequency of 0.01431 and the presence of two homozygous individuals. The probability of Loss-of-function Intolerance (pLI) for *IRAK2* is zero, indicating tolerance to heterozygous predicted Loss-of-Function (pLoF) variation at the gene level. Accordingly, the large number of heterozygous *IRAK2-Δex2* carriers observed in gnomAD SVs v4.1.0 and in our study is expected and consistent with an autosomal recessive model for *IRAK2* LoF mutation. In all eleven unrelated pedigrees, disease status segregated strictly with biallelic

inheritance of *IRAK2-Δex2*, which is fully compatible with an autosomal recessive mechanism. We also demonstrated that two previously reported *IRAK2* SNVs preserve NF-κB signaling activity, which are classified as benign variants.

Given the broad phenotypic spectrum of DIRAK2, including immunodeficiency, autoimmunity, and autoinflammatory manifestations, and the identification of twelve affected individuals in this study, it is likely that a substantial number of cases of PID, SLE, and inflammatory bowel disease (IBD) were previously misdiagnosed or unrecognized prior to the identification of DIRAK2. The higher prevalence of the *IRAK2-Δex2* CNV in the East Asian population further suggests that DIRAK2 may be an underrecognized cause of immune dysregulation in this population.

Pathogenic mutations in genes involved in TLRs signaling pathways result in a wide range of immune disorders. MyD88- or IRAK4-deficient individuals display a susceptibility to pyogenic infections due to impaired TLR and interleukin-1 receptor (IL-1R) signaling[15,16]. Two patients in our study were diagnosed with PIDs, consistent with MyD88 or IRAK4 deficiencies. TLR4 deficiency has been associated with impaired responses to LPS and Crohn's disease[10], which was consistent with the phenotypes observed in P8 and P9 in our study. Some patients with IRAK4 deficiency also develop autoimmune or autoinflammatory diseases sharing clinical manifestations with DIRAK2, including autoantibody production, autoinflammation, and anemia[17-20]. NF-κB signaling is essential for maintaining immune tolerance and homeostasis[21]. Studies in humans and mice have shown that RELB deficiency leads to dysregulated inflammatory gene expression and immune tolerance breakdown due to NF-κB imbalance[22,23]. Collectively, these findings suggest that impaired TLR-Myddosome-NF-κB signaling may contribute to the development of autoimmune and autoinflammatory manifestations.

SLE is closely associated with increased type I IFN activity[24]. Gain-of-function mutations in *TMEM173* and *DDX58* lead to lupus-like phenotypes and lupus nephritis, respectively, both exhibiting elevated IFN signatures[25,26]. Several patients with DIRAK2 in our study also demonstrated elevated baseline IFN signatures, including four individuals diagnosed with SLE accompanied by lupus nephritis. scRNA-seq revealed that the IFN signature was upregulated in inflammatory monocytes. This finding was corroborated in both BMDMs and PMA-differentiated THP-1 cell lines, suggesting a mechanistic link between DIRAK2 and aberrant IFN signaling. These data suggest that the type I IFN signature may serve as a biomarker for disease activity and severity in DIRAK2 with autoimmunity. Notably, blockade of the type I IFN pathway, via neutralization of IFN-α, inhibition of IFNAR, or downstream modulation of the JAK-STAT cascade, has emerged as a therapeutic strategy under active evaluation in SLE[24,27]. Selective JAK/TYK2 inhibitors are being evaluated in late-phase clinical trials for SLE. Given the IFN-associated immune phenotype observed in several patients in our study, modulation of this pathway may offer a rationale for future exploration in DIRAK2 patients with autoimmune features. Nevertheless, careful preclinical and clinical studies are required to define the safety, feasibility, and potential benefit of such approaches.

In summary, we report the identification of IRAK2 deficiency as a cause of immune dysregulation. DIRAK2 leads to impaired NF-κB signaling and is associated with a potentially elevated type I IFN signature in some patients (Supplementary Fig. 11). Our study highlights the critical role and dual function of IRAK2 in regulating inflammatory responses and provides insights into the pathogenesis of DIRAK2.

Methods

Patients

All patients enrolled in the study were evaluated under protocols approved by the Institutional Review Boards of the Children's Hospital, Zhejiang University School of Medicine (2021-IRB-0172-Y-02), and Jinling Hospital (2022DZKY-061-01). Written informed consents were obtained from all participants or their legal guardians. This study was conducted in accordance with relevant ethical regulations and guidelines. Given the mechanistic focus of this study, sex and/or gender was not included as variables in the study design or analysis. Routine clinical data were obtained through retrospective chart review.

Cell lines, cell culture, and treatment

The HEK293T and THP-1 cell lines were obtained from the American Type Culture Collection (ATCC). HEK293T cells and bone marrow-derived macrophages (BMDMs) were cultured in DMEM (C11995500BT, Gibco) supplemented with 10% FBS (F103, Vazyme). Peripheral blood mononuclear cells (PBMCs) were cultured in RPMI-1640 (C11875500BT, Gibco) supplemented with 10% FBS (F103, Vazyme). THP-1 cells were cultured in RPMI-1640 (C11875500BT, Gibco) supplemented with 10% FBS (F103, Vazyme) and 50 μM β-mercaptoethanol (M6250, Sigma). A stable HEK293T-TLR4 cell line was established through lentiviral transduction of TLR4-HA, CD14-Flag, and LY96[28-31]. IRAK2-WT and IRAK2-Δex2 were stably expressed in THP-1 cell lines via lentiviral transduction.

IRAK2 KO HEK293T and THP-1 cells were generated using the CRISPR/Cas9 system[32] with the following single guide RNAs, sgRNA-1#: 5'-CATGGACGCGCTCAGCGAGT**GGG**-3', sgRNA-2#: 5'-GCCGGCCCCGTAGCG TGCCA**TGG**-3', sgRNA-3#: 5'-CAGGTCTGTGATCACGTAGG**AGG**-3', and sgRNA-4#: 5'-CCTGAACTGTGAGTAACTCA**GGG**-3' (PAM highlighted in bold). The pSpCas9(BB)-2A-Puro (PX459) plasmids carrying *IRAK2*-specific sgRNAs were transfected into HEK293T and THP-1 cells using Lipofectamine 3000 (L3000015, Invitrogen) according to the manufacturer's instructions. Following the transfection, cells were subjected to selection with 1

μg/mL puromycin (ST551, Beyotime) for five days. Viable single cells were sorted using a Beckman Moflo Astrios EQ sorter, and monoclonal cell lines were subsequently cultivated and genotyped in 96-well plates. Selected KO cell clones were confirmed to contain biallelic frameshift mutations with no detectable WT sequences, as verified by Sanger sequencing.

The stable HEK293T-TLR4 cell line was stimulated with 1 μg/mL LPS (L6529, Sigma) for specified durations. PBMCs were stimulated with 1 μg/mL LPS (L6529, Sigma) for 8 hours for scRNA-seq and 12 hours for CyTOF and Cytometric Bead Array (CBA) (551811, BD Biosciences) at the density of 1.5×10^6 cells/mL. BMDMs were stimulated with 100 ng/mL LPS (L6529, Sigma), 25 ng/mL R848 (HY-13740, MCE), 50 ng/mL FSL-1 (HY-P2036, MCE), 1 μg/mL PAM3 (ab142085-100ug, Abcam), and 2 μM ODN2006 (Tsingke), respectively, for 8 hours prior to RNA extraction. BMDMs were stimulated with 5 μg/mL poly(I:C) (HY-107202, MCE) for 4 hours prior to RNA extraction. PMA-differentiated THP-1 cell lines were stimulated with 10 ng/mL LPS (L6529, Sigma) for specified durations. PMA-differentiated THP-1 cell lines and PBMCs were treated with 0.5 μM Baricitinib (LY3009104, MCE) for 12 hours. PMA-differentiated THP-1 cells were pretreated with TIRAP inhibitor (NBP2-29331, Novus; 10 μM for 2 hours), TRIF inhibitor (HY-P2565, MCE; 10 μM for 2 hours), TBK1/IKKε inhibitor (HY-12453, MCE; 1 μM for 30 minutes), or TAK1 inhibitor (HY-12686, MCE; 100 nM for 30 minutes) prior to LPS stimulation.

PMA-induced differentiation of THP-1 cells

In this study, THP-1 cells were pretreated with PMA before all experiments. Cells were seeded at a density of 1×10^6 cells/mL. Differentiation was induced by treating the cells with 100 ng/mL PMA (P8139, Sigma) for 48 hours. After 24 hours, the medium was replaced with fresh culture medium containing 100 ng/mL PMA to ensure continued differentiation. Then cells were ready for subsequent analyses.

siRNA-mediated gene knockdown in THP-1 cells

TICAM1 (TRIF) was knocked down in undifferentiated THP-1 cells using the ProteanFect Transfection Kit (PT01, Nanoportal Biotech). siRNAs were synthesized by Tsingke Biotechnology. The siRNAs targeting human *TICAM1* was as follows:

siRNA#1: sense, 5'-GAAGAUACCACCUCUCCAA(dT)(dT)-3'; antisense, 5'-UUGGAGAGGUGGUAUCUUC(dT)(dT)-3';

siRNA#2: sense, 5'-CUUCGACAUUCUAGGUGCA(dT)(dT)-3'; antisense, 5'-UGCACCUAGAAUGUCGAAG(dT)(dT)-3'.

For one well of a 24-well plate, THP-1 cells were passaged 24 hours before transfection. Cells were collected, washed once with Opti-MEM to remove residual serum, and resuspended in Opti-MEM at 0.5-1×10^7 cells/mL. siRNA (200 pmol) was mixed with 200 μL Reagent A, followed by addition of 7 μL Reagent B and vortexing for 10 s. The transfection mixture was combined with 100 μL cell suspension and incubated at 37 ℃ for 45-60 minutes. Transfection was terminated by adding 1 mL complete medium, followed by centrifuging at 300 x g for 5 minutes. Cells were resuspended in complete medium and allowed to recover for 2 hours, then differentiated with PMA for 48 hours. Knockdown efficiency was assessed by qPCR and immunoblotting.

Mice

Irak2$^{\Delta ex2/\Delta ex2}$ mice were generated on a C57BL/6JGpt background by GemPharmatech Co.,Ltd. (Nanjing, China) using CRISPR/Cas9 technology[32] to delete exon 2 of *Irak2* gene in the mouse genome. The sgRNAs targeting *Irak2* are as follows: sgRNA-5S2#: 5'-GGTAGATGGGAACCCTCCCT**TGG**-3' and sgRNA-3S2#: 5'-GTTAGGAGACG GTAAGCAGC**AGG**-3' (PAM highlighted in bold). All mice were maintained in a SPF conditions with a 12-hour light/12-hour dark cycle, controlled ambient temperature (20-26 ℃), and relative

humidity (40-70%). Mice were euthanized by CO_2 inhalation or cervical dislocation, in accordance with institutional animal care guidelines. For mechanistic and disease-phenotyping experiments, female mice with age-matched WT littermate controls were used. Both male and female mice were included in LPS-challenged survival analyses. The animals used in this study adhered to all relevant ethical regulations for animal research and were age- and sex- matched. All experimental protocols involving animals were approved by Zhejiang University's Institutional Animal Care and Use Committee (AP CODE: ZJU20240500).

Induction of BMDMs *ex vivo*

After CO_2 euthanasia, bone marrow cells were harvested from the femurs and tibias of WT or *Irak2*$^{\Delta ex2/\Delta ex2}$ mice. These cells were then cultured in DMEM supplemented with 10% FBS, 1% penicillin/streptomycin (15140122, Gibco), and 10 ng/mL mouse M-CSF (315-02, PeproTech) for up to 6 days. The adherent BMDMs were subsequently utilized for further analyses.

Analysis of *in vivo* response to LPS

Age- and sex-matched mice were injected intraperitoneally (i.p.) with PBS or LPS (dose specified in the text and figure legends)[33]. After 2 hours, serum was collected for cytokine analysis using the ABplex Mouse Cytokine 15-Plex Assay Kit (RK05203, Abclonal) following the manufacturer's instruction. After 2 hours, the liver, spleen, and kidney were harvested for mRNA analysis via quantitative RT-PCR. After 2 hours, liver tissues were fixed in 4% paraformaldehyde fix solution (E672002, Sangon Biotech), stained with hematoxylin and eosin, and processed by HaoKe biotechnology Co., Ltd.

Mice were injected with high dose LPS (20 mg/kg) for survival analysis. Survival was monitored at regular intervals over a 7-day period. Kaplan-Meier survival curves were generated and compared using the log-rank test.

E. coli infection model in mice

Kanamycin-resistant *E. coli* (BNCC352083; BeNa Culture Collection) was harvested by centrifugation at 2,000 x g for 10 minutes, washed twice with PBS, and resuspended in PBS. The optical density at 600 nm (OD_{600}) was measured (PBS blank), and bacterial concentration was estimated assuming OD_{600} = 0.1 for 1×10^8 CFU/mL[34].

Age and sex-matched mice were injected i.p. with a sublethal dose of live *E. coli* (5×10^8 CFU in 0.5 mL PBS). The injection site was disinfected with 70% ethanol. At 2 hours post-injection, blood was collected from the tail vein and serum was isolated. Serum Tnf and Il-10 levels were quantified by ELISA (Tnf: EK282; Il-10: EK210, Lianke Bio). Mice were euthanized by cervical dislocation 4 hours post-injection. The peritoneal cavity was lavaged with 5 mL PBS, and lavage fluid was collected. Samples were serially diluted, plated on LB agar containing kanamycin, and incubated overnight at 37 ℃. Bacterial burden was calculated as CFU/mL based on colony counts.

Whole exome sequencing

Maxwell RSC Whole Blood DNA Kit (AS1520, Promega) was employed to extract DNA from whole blood samples. One microgram of DNA was utilized for whole exome sequencing (WES). The sequencing and subsequent data analysis were conducted according to previously established protocols[35]. For analysis of single nucleotide variants (SNVs) or small insertions and deletions (indels), variants were annotated utilizing ANNOVAR (2019Oct24). We removed high-frequency variants presenting in the gnomAD, ClinVar, Kaviar, dbSNP, and an in-house database. Furthermore, variants were screened based on recessive or *de novo* inheritance patterns. In addition, we identified CNVs by performing the germline CNVs detection pipeline of Genome Analysis Toolkit 4 (GATK4).

Whole genome sequencing

Genomic DNA extraction was performed as described in the WES section. Whole-genome libraries were constructed and sequenced by Novogene (Beijing, China) on the Illumina NovaSeq 6000 platform with 150 bp paired-end reads. Variant calling for SNVs, indels, and CNVs in the whole genome sequencing (WGS) data was performed using the same tools as those used in the WES analysis.

Sanger sequencing

Sanger sequencing was used to confirm the *IRAK2-*Δ*ex2* mutation identified by WES or WGS. For genomic DNA, two pairs were designed. Pair 1 (Fwd: 5'-GCTCCCTGCAAGTTTTGTCCCATA-3'; Rvs: 5'-CCTTGGCAACTAAGGCTGAGGAAA-3') flanks the genomic breakpoints. Pair 2 (Fwd: 5'-CCCAGCTGCGGAAGATCAAGT-3'; Rvs: 5'-CCTTGGCAACTAAGGCTGAGGAAA-3') includes a forward primer located within the exon 2. The primers for human cDNA were as follows. Fwd: 5'-ATGGCCTGCTACATCTACCAGCTG-3'; Rvs: 5'-GCTGAAGTCCTTTGAATCAGACGAAG-3'.

Antibodies and expression plasmids

The following antibodies were purchased from Cell Signaling Technology: p-p65 (Ser536) (#3033; 1:1000), p65 (#8242; 1:1000), p-p38 (Thr180/Tyr182) (#4511; 1:1000), p38 (#8690; 1:1000), HA-tag (#3724S; 1:1000), p-p105 (Ser932) (#4806; 1:1000), p105 (#4717; 1:1000), p-JNK (Thr183/Tyr185) (#4668; 1:1000), JNK (#9252; 1:1000), IRF3 (#4302; 1:1000), p-STAT1 (Tyr701) (#9167; 1:1000), STAT1 (#14994; 1:1000), p-STAT2 (Tyr690) (#88410; 1:1000), STAT2 (#72604; 1:1000), β-ACTIN (#4970; 1:1000), p-IKKε (Ser172) (#8766; 1:1000), IKKε (#2905; 1:1000), p-TBK1 (Ser172) (#5483; 1:1000), TBK1 (#3504; 1:1000), TRIF (#16809; 1:1000). Flag-tag (MA1-91878; 1:3000) was purchased from -Aldrich. Myc-tag (60003-2-Ig; 1:3000) and HRP-conjugated

GAPDH (HRP-60004; 1:3000) were purchased from Proteintech. Myc-tag (S0B0383; 1:3000) was purchased from STARTER. p-IRF3 (Ser386) (AP0995; 1:1000) was purchased from Abclonal.

Human WT *IRAK2*, *IRAK4*, *TRAF6*, *TLR4*, *CD14*, *LY96*, the mutant *IRAK2*-Δ*ex2*, and the *IRAK2* variants Q68AfsTer31, V35M, S47Y, R50Q, A69D, L78P, R312G, T410M, and R506W were engineered by cloning the corresponding human cDNA into pLentiCMV lentiviral expression vector. The vectors were constructed in-house and designed for stable or transient gene expression in mammalian cells. Constructs were generated with or without an epitope tag, with all tags positioned at the C-terminus of the encoded proteins. The pLentiCMV backbone is compatible with second-generation lentiviral packaging system.

Transfection

Transient transfection of plasmids into HEK293T cells was carried out using Lipofectamine 2000 (11668019, Invitrogen), following the manufacturer's instructions. Cells were harvested 24 to 30 hours post-transfection.

Western blotting and co-immunoprecipitation

Cells were lysed using cold cell lysis buffer (20 mM Tris-HCl pH 7.4, 150 mM NaCl, 0.5% NP-40) along with cOmplete protease inhibitor cocktail (04693159001, Roche) and PhosSTOP (04906837001, Roche). The lysate was vortexed intermittently every 10 minutes for a total of three times. Subsequently, it was centrifuged at 12,000 x g for 10 minutes at 4 ℃. The supernatants were collected for the protein concentration determination using BCA protein assay kit (23225, Thermo Fisher).

Proteins were separated on 8% or 10% SDS-PAGE gels and then transferred onto a 0.45 μm PVDF membrane. The membrane was then probed using specific primary and secondary antibodies. Protein bands were detected and analyzed with the Odyssey infrared imaging system (LI-COR Biosciences) and the ImageQuant 800 (Cytiva). Uncropped and unprocessed blot scans are provided in the Source Data file.

For co-immunoprecipitation (co-IP), the protein concentration-adjusted cell lysates were incubated with DYKDDDDK tag Nanoselector Magnetic beads (016-101-003, AlpVHHS) at 4 ℃ overnight. Subsequently, the beads were washed five times with lysis buffer and one time with high-salt buffer (20 mM Tris-HCl pH 7.4, 500 mM NaCl, 0.5% NP-40). The complexes were analyzed by Western blotting and mass spectrometry.

Mass spectrometry

The co-IP eluates were resolved by SDS-PAGE and stained with 0.1% Coomassie Brilliant Blue G-250 (#1610406, Bio-Rad) in 30% ethanol and 10% acetic acid for 30 minutes. Gels were destained three times in destaining buffer (30% ethanol and 10% acetic acid) overnight. Gel bands corresponding to the expected molecular weight were excised into pieces smaller than 1×1 cm^2. Excised gel pieces were then destained, reduced with dithiothreitol, alkylated with iodoacetamide, and digested with trypsin at 37 ℃ overnight. Peptides were extracted with 60% acetonitrile/0.1% trifluoroacetic acid, dried, and reconstituted in 2% formic acid for LC-MS analysis.

Peptides were separated on a nanoElute system (Bruker) with an EASY-Spray HPLC column (ES906, Thermo Fisher). Mobile phases were 0.1% formic acid in water (solvent A) and 0.1% formic acid in acetonitrile (solvent B). The column was equilibrated with 95% solvent A. Peptides

were eluted at 300 nL/minute over a 30-minute gradient from 5% to 35% solvent B for 18 minutes, 35% to 80% solvent B for 2 minutes, and 80% solvent B for 10 minutes.

Eluted peptides were analyzed on a timsTOF Pro mass spectrometer (Bruker) in positive ion mode with parallel accumulation serial fragmentation (PASEF) mode. Precursors and fragments were analyzed at the TOF detector over a mass range of m/z (mass-to-charge ratio) 100-1700 with a cycle time of 0.95 s, consisting of 1 MS and 8 PASEF MS/MS scans. The electrospray voltage was set to 1.5 kV, and active exclusion was enabled with a release time of 24 s. MS .d folder was analyzed with MZmine v4.9.14[36].

Luciferase assay

NF-κB luciferase reporter plasmid (pGL4.32(NF-κB-RE)) and Renilla luciferase expression plasmid (pRL-TK), along with pLentiCMV-IRAK2-Myc expression plasmids, were co-transfected into HEK293T-*IRAK2* KO cells. Cells were harvested 24 hours post-transfection, and luciferase activity was measured using a multimode plate reader (BioTek). Data were analyzed as fold induction, with Firefly luciferase activity normalized to Renilla luciferase activity.

Cytokine detection

Serum or supernatants of PBMCs were analyzed using BD Cytometric Bead Array (551811, BD Biosciences) to quantify concentrations of cytokines and chemokines. Data analysis was conducted using the FCAP Array V3 software (BD Biosciences).

Protein structure modeling

An illustration of the interaction between the death domains of IRAK2 and IRAK4, based on data from the Protein Data Bank (3MOP)[2], was prepared using UCSF ChimeraX (version 1.11.0)[37]. Molecular graphics and analyses performed with UCSF ChimeraX, developed by the Resource

for Biocomputing, Visualization, and Informatics at the University of California, San Francisco, with support from National Institutes of Health R01-GM129325 and the Office of Cyber Infrastructure and Computational Biology, National Institute of Allergy and Infectious Diseases.

Quantitative real-time PCR

BMDMs, PMA-differentiated THP-1 cells, and PBMCs were subjected to specific treatments indicated in the figure legends prior to cell harvesting. Then total RNA was extracted utilizing the RNeasy Mini Kit (74104, Qiagen). cDNA was generated by HiScript III All-in-one RT SuperMix (R333-01, Vazyme) following manufacturer's instruction. And quantitative real-time PCR (qPCR) was performed by using 2× Universal SYBR Green Fast qPCR Mix (RK21203, ABclonal), running on ROCHE LightCycler 480II system. Relative mRNA levels were quantified using the $\Delta\Delta Ct$ method.

The following primer sets were used to detect gene expression in mouse. *Actb*: Fwd: 5'-GGCTGTATTCCCCTCCATCG-3', Rvs: 5'-CCAGTTGGTAACAATGCCATGT-3'; *Tnf*: Fwd: 5'-GACGTGGAACTGGCAGAAGAG-3', Rvs: 5'-TTGGTGGTTTGTGAGTGTGAG-3'; *Tnfaip3*: Fwd: 5'-ACAGTGGACCTGGTAAGAAAACA-3', Rvs: 5'-CCTCCGTGACTGAT GACAAGAT-3'; *Il6*: Fwd: 5'-CCAAGAGGTGAGTGCTTCCC-3', Rvs: 5'-CTGTTGTTCAG ACTCTCTCCCT-3'; *Il10*: Fwd: 5'- GCTCTTACTGACTGGCATGAG-3', Rvs: 5'-CGCAGC TCTAGGAGCATGTG-3'; *Ifnb1*: Fwd: 5'-CAGCTCCAAGAAAGGACGAAC-3', Rvs: 5'-GGCAGTGTAACTCTTCTGCAT-3'; *Il1b*: Fwd: 5'-GAAATGCCACCTTTTGACAGTG-3', Rvs: 5'-TGGATGCTCTCATCAGGACAG-3'; *Ifit1*: Fwd: 5'-CTGAGATGTCACTTCACATG GAA-3', Rvs: 5'-GTGCATCCCCAATGGGTTCT-3'; *Ifit3*: Fwd: 5'-CCTACATAAAGCAC CTAGATGGC-3', Rvs: 5'-ATGTGATAGTAGATCCAGGCGT-3'; *Irak2*: Fwd: 5'-GCCCCTT GTTCCCTGAAAACT-3', Rvs: 5'-CTCGCTGATTCGGTGGCTT-3'; *Irak2-ex2*: Fwd: 5'-GGACGACCTGTGCCGCAATATC-3', Rvs: 5'-

TGGGCAGCTCGGTAGAGTTC-3'; *Nfkbia*: Fwd: 5'-TGAAGGACGAGGAGTACGAGC-3', Rvs: 5'-TTCGTGGATGATTGCCAAGTG-3'.

The following primer sets were used to detect gene expression in human. *GAPDH*: Fwd: 5'-GGAGCGAGATCCCTCCAAAAT-3', Rvs: 5'-GGCTGTTGTCATACTTCTCATGG-3'; *ACTB*: Fwd: 5'-CATGTACGTTGCTATCCAGGC-3', Rvs: 5'- CTCCTTAAT GTCACGCACGAT-3'; *IFNB1* : Fwd: 5'-GCTTGGATTCCTACAAAGAAGCA-3', Rvs: 5'-ATAGATGGTCAATGCGGCGTC-3'; *ISG15*: Fwd: 5'-CGCAGATCACCCAGAAGATCG-3', Rvs: 5'-TTCGTCGCATTTGTCCACCA-3'; *IFIT1*: Fwd: 5'-TTGATGACGATGAAAT GCCTGA-3', Rvs: 5'-CAGGTCACCAGACTCCTCAC-3'; *IFIT3*: Fwd: 5'-TCAGAA GTCTAGTCACTTGGGG-3', Rvs: 5'-ACACCTTCGCCCTTTCATTTC-3'; *IRAK2*: Fwd: 5'-CCAGGCAACCGATGACTTCAA-3', Rvs: 5'-TGGGGTGGCAGCATCTAAGA-3'; *IRAK2-ex2*: Fwd: 5'-CCCAGCTGCGGAAGATCAAGT-3', Rvs: 5'-GCCTTTCTTACA GAAGCTGCCAAAGG-3'; *TICAM1*: Fwd: 5'-CCTGGAATCATCATCGGAACAG-3', Rvs: 5'-TGAGTGGTCTATGGCGTCCT-3'; *NFKBIA*: Fwd: 5'-CTCCGAGACTTTCGA GGAAATAC-3', Rvs: 5'-GCCATTGTAGTTGGTAGCCTTCA-3'; *IL10*: Fwd: 5'-GACTTTAAGGGTTACCTGGGTTG-3', Rvs: 5'-TCACATGCGCCTTGATGTCTG-3'; *IL1B*: Fwd: 5'-ATGATGGCTTATTACAGTGGCAA-3', Rvs: 5'-GTCGGAGATTCGTAGCTGGA-3'; *TNFAIP3*: Fwd: 5'-TCCTCAGGCTTTGTATTTGAGC-3', Rvs: 5'-TGTGTATCGGTGCATGGTTTTA-3'.

Bulk RNA sequencing

One microgram of RNA was used for library construction using NEBNext Ultra RNA library Prep Kit for Illumina (New England Biolabs). Sequencing was subsequently performed on Illumina Novaseq (San Diega, CA). We used HISAT2 to map sequenced reads to the human reference genome (GRCh38). The reads numbers for each gene were counted using featureCounts. We used the R package DESeq2 to perform differential gene expression analysis. GSEA[38] was performed to explore aberrantly activated signaling in patients' PBMCs.

Single-cell RNA sequencing and data processing

10× Genomics Chromium machine was used for 8,000-10,000 single cell capture. The cDNA was subsequently amplified through PCR. Library construction and sequencing were conducted as previously described[39]. scRNA-seq data were aligned with the GRCh38 human reference genome and quantified by CellRanger (version 7.1.0, 10× Genomics).

R package Seurat (version 4.4.0)[40] was used for downstream analysis. We calculated the percentages of mitochondrial UMI counts. For high-quality cell filtering, cells expressing fewer than 300 genes, cells with more than 7,500 detected genes, and cells with more than 15% mitochondrial UMI counts were removed. Genes expressed in fewer than three cells were excluded. The gene count expression profile was normalized using the LogNormalize method with a scale factor 10,000, and the top 2,000 highly variable genes were identified using the FindVariableFeatures function. Next, we applied ScaleData function to scale data. Principal component analysis was performed on the scaled data using the RunPCA function with default parameters. RunHarmony function in the R package harmony (version 1.2.0)[41] was used for batch correction. We constructed a shared nearest neighbor graph using the FindNeighbors function and clustered cells using the Louvain algorithm with the FindClusters function based on the harmony reduction. Finally, a total of 104,028 cells were obtained. Differentially expressed genes between clusters were identified using the FindAllMarkers and FindConservedMarkers functions for cell annotation. RunUMAP function facilitated the visualization of cell clustering.

Marker genes associated with the myeloid cell lineage, specifically for monocytes, including *CD14*, *S100A8*, *HES1*, *IL1B*, *CD68*, *HIF1A*, *EGR1*, *ANPEP*, *VEGFA*, *NLRP3*, *MNDA*, and *CXCL8*[42-50], were used to define inflammatory monocytes.

Estimation of cell differentiation state and pseudotime inference

We utilized the R package CytoTRACE (version 0.3.3)[51] to predict cellular differentiation status. CytoTRACE is an unsupervised computational framework designed to assess relative differentiation states based on single-cell transcriptomic data. The algorithm generates a rank score, where a lower rank score indicates a more differentiated cell state.

We used three different algorithms: Slingshot, Diffusion Map and SCORPIUS (version 1.0.9)[40,52,53] to infer pseudotime. Slingshot combines highly stable techniques necessary for noisy single-cell data with the flexibility to identify multiple lineages under varying levels of supervision. It computes pseudotime by constructing simultaneous principal curves and performing orthogonal projection through the R package slingshot (version 2.12.0). The function 'sc.tl.diffmap' in the Python package scanpy (version 1.10.3) was used to compute 'DPT_time', which represents the use of the Diffusion Map algorithm, a non-linear dimensionality reduction method that captures the dynamics of the divergence more accurately. SCORPIUS, an approach for inferring linear developmental chronologies by reconstructing linear dynamic processes.

Cytometry by time of flight

For mass cytometry analysis, purified antibodies were purchased from BioLegend, Thermo Fisher, Bio-Rad, and R&D Systems using the clones detailed in Supplementary Table 5. Antibodies were conjugated to the indicated metal tags using the MaxPAR antibody labelling kit (Fluidigm). All labeled antibodies were titrated to determine the optimal working concentration before use.

PBMCs from P3, P4, and three unaffected controls were freshly prepared from whole blood. Cell count and viability were assessed with a Countess II FL automated cell counter (Thermo Fisher), and samples with viability greater than 90% were used. PBMCs were washed once with PBS and resuspended in 300 µL cold PBS at 1.5×10^6 cells per sample. Cells were incubated with 100 µL

of 250 nM cisplatin (Fluidigm) for 5 minutes on ice, followed by Fc blocking for 30 minutes on ice and surface antibody staining for 30 minutes on ice. After two washes with FACS buffer (0.5% BSA in 1×PBS), cells were fixed overnight in 200 µL intercalation solution consisting of Maxpar Fix and Perm Buffer containing 250 nM 191/193Ir (Fluidigm). Cells were then washed twice, permeabilized with Perm Buffer III (558050, BD Biosciences), and stained with intracellular antibodies for 30 minutes on ice. After washing, cells were resuspended in deionized water containing 20% EQ beads (Fluidigm) and acquired on a Helios mass cytometer (Fluidigm).

The Cytometry by time of flight (CyTOF) data from P3, P4, and three unaffected controls were exported as Flow Cytometry Standard (FCS) files, which were then standardized and debarcoded using the NolanLab Beads Normalizer package (version 0.3). All FCS files were manually gated in FlowJo (version 10.0.7) to remove doublets. $CD45^+$ single cells were identified based on DNA markers (191Ir and 193Ir), 194Pt, and event length. From each sample, 10,000 cells were randomly selected for downstream analysis. Downstream reading, transformation, and t-SNE dimensionality reduction of the FCS files were performed following the previously published pipeline[39].

The algorithm of interferon score

Firstly, 28 genes related to IFN response were selected from the previous study[54]. They were: *CXCL10*, *DDX60*, *EPSTI1*, *GBP1*, *HERC5*, *HERC6*, *IFI27*, *IFI44*, *IFI44L*, *IFI6*, *IFIT1*, *IFIT2*, *IFIT3*, *IFIT5*, *ISG15*, *LAMP3*, *LY6E*, *MX1*, *OAS1*, *OAS2*, *OAS3*, *OASL*, *RSAD2*, *RTP4*, *SIGLEC1*, *SOCS1*, *SPATS2L*, and *USP18*. Secondly, we calculated the z-scores of each 28 genes with DESeq2 (1.44.0) normalized reads counts using the mean and standard deviation of controls. Subsequently, for each sample, we summed the 28 z-scores as their IFN response scores.

Calculation of signature score for scRNA-seq

To evaluate the immune response among individuals for the given cell type, we used the R package AUCell (version 1.26.0)[55] to calculate to signature score for NF-κB and type I IFN. AUCell is ranked-based, which is independent of gene expression units and the normalized method. The NF-κB gene set was obtained from the resource [https://www.bu.edu/nf-kb/gene-resources/target-genes/], including cytokines, chemokines, immune receptors, etc. Type I IFN gene set was collected from previous report[54].

Flow cytometry analysis of phosphorylation

For detection of phosphorylated protein, a total of 1.0×10^6 freshly isolated PBMCs were used for each assay. Cell counts and viability were determined using a Countess II FL automated cell counter (Thermo Fisher) with 0.4% Trypan Blue, and the viability of PBMCs in all samples exceeded 90%. PBMCs were permeabilized using Perm Buffer III (558050, BD Biosciences). Cells were then stained with an antibody against p-IRF3 (Ser386) (#37829, CST) followed by Alexa Fluor 647-conjugated anti-rabbit IgG (H+L) (a-31573, Thermo Fisher). Data were acquired on a CytoFLEX LX flow cytometer and analyzed using FlowJo (version 10.8) Software (BD Life Sciences).

Statistics and Reproducibility

Statistical analyses were performed using GraphPad Prism. The standard error of the mean (SEM) was used to represent variability across independent biological samples. For comparisons between two independent groups, a two-sided unpaired *t*-test with Welch's correction was used. For comparisons among multiple groups, one-way ANOVA followed by Dunnett's multiple comparisons test was performed. For experiments with multiple factors, two-way ANOVA with Tukey's or Šídák's multiple comparisons correction was applied, as appropriate. For non-normally distributed data or small sample sizes, the two-sided Wilcoxon rank-sum test was used. A *P* value < 0.05 was considered statistically significant. Statistical analyses of bulk RNA sequencing,

CyTOF, and scRNA-seq were performed using R 4.4.0 as detailed in the relevant sections and legends. All experiments were independently repeated at least three times with similar results. Exact *P* values and Source data are provided in the Source data file.

Web Resources

The URLs for data presented herein are as follows:

gnomAD, https://gnomad.broadinstitute.org/

PDB, https://www.rcsb.org/

Data Availability

The raw bulk RNA sequencing and scRNA-seq data, together with the raw WES/WGS data generated in this study, have been deposited in the Genome Sequence Archive in National Genomics Data Center, China National Center for Bioinformation/Beijing Institute of Genomics, Chinese Academy of Sciences (GSA-Human) under accession code: HRA018055 [https://ngdc.cncb.ac.cn/gsa-human/browse/HRA018055] and HRA018317 [https://ngdc.cncb.ac.cn/gsa-human/browse/HRA018317], respectively. All other data within the article or the Supplementary Information are available from the corresponding author on request. Source data are provided with this paper.

Code Availability

The code for this paper is available on GitHub [https://github.com/shuangyuema95-glitch/IRAK2025] and Zenodo [https://doi.org/10.5281/zenodo.17136147].

References

1. Fitzgerald, K.A. & Kagan, J.C. Toll-like Receptors and the Control of Immunity. *Cell* **180**, 1044-1066 (2020).
2. Lin, S.C., Lo, Y.C. & Wu, H. Helical assembly in the MyD88-IRAK4-IRAK2 complex in TLR/IL-1R signalling. *Nature* **465**, 885-90 (2010).
3. Kawagoe, T. *et al.* Sequential control of Toll-like receptor-dependent responses by IRAK1 and IRAK2. *Nat Immunol* **9**, 684-91 (2008).
4. Kawai, T. & Akira, S. The role of pattern-recognition receptors in innate immunity: update on Toll-like receptors. *Nat Immunol* **11**, 373-84 (2010).
5. Amali, A.A. *et al.* Severe invasive infections linked to IRAK2 immune variants. *Int J Infect Dis* **148**, 107245 (2024).
6. Wan, Y. *et al.* Interleukin-1 receptor-associated kinase 2 is critical for lipopolysaccharide-mediated post-transcriptional control. *J Biol Chem* **284**, 10367-75 (2009).
7. Hamesch, K., Borkham-Kamphorst, E., Strnad, P. & Weiskirchen, R. Lipopolysaccharide-induced inflammatory liver injury in mice. *Lab Anim* **49**, 37-46 (2015).
8. Hardy, M.P. & O'Neill, L.A. The murine IRAK2 gene encodes four alternatively spliced isoforms, two of which are inhibitory. *J Biol Chem* **279**, 27699-708 (2004).
9. Kolumam, G.A., Thomas, S., Thompson, L.J., Sprent, J. & Murali-Krishna, K. Type I interferons act directly on CD8 T cells to allow clonal expansion and memory formation in response to viral infection. *J Exp Med* **202**, 637-50 (2005).
10. Capitani, M. *et al.* Biallelic TLR4 deficiency in humans. *J Allergy Clin Immunol* **151**, 783-790 e5 (2023).
11. Mishra, B. *et al.* IL-10 targets IRF transcription factors to suppress IFN and inflammatory response genes by epigenetic mechanisms. *Nat Immunol* **26**, 748-759 (2025).
12. Merour, E. *et al.* A20 (tnfaip3) is a negative feedback regulator of RIG-I-Mediated IFN induction in teleost. *Fish Shellfish Immunol* **84**, 857-864 (2019).
13. Saitoh, T. *et al.* A20 is a negative regulator of IFN regulatory factor 3 signaling. *J Immunol* **174**, 1507-12 (2005).
14. Franke, G. *et al.* Alu-Alu recombination underlies the vast majority of large VHL germline deletions: Molecular characterization and genotype-phenotype correlations in VHL patients. *Hum Mutat* **30**, 776-86 (2009).
15. von Bernuth, H. *et al.* Pyogenic bacterial infections in humans with MyD88 deficiency. *Science* **321**, 691-6 (2008).
16. Picard, C. *et al.* Pyogenic bacterial infections in humans with IRAK-4 deficiency. *Science* **299**, 2076-9 (2003).
17. Nishimura, S. *et al.* IRAK4 Deficiency Presenting with Anti-NMDAR Encephalitis and HHV6 Reactivation. *J Clin Immunol* **41**, 125-135 (2021).
18. Hugle, B., Handel, N., Schwarz, K., Borte, M. & Schuster, V. Antinuclear Antibody-Positive Juvenile Idiopathic Arthritis Despite IRAK-4 Deficiency. *J Clin Immunol* **38**, 450-453 (2018).
19. Cooray, S. *et al.* Neuroinflammation, autoinflammation, splenomegaly and anemia caused by bi-allelic mutations in IRAK4. *Front Immunol* **14**, 1231749 (2023).
20. Gonzales, J.A., Nortey, J., Reddy, A., Doan, T. & Acharya, N.R. Intraocular Inflammation Associated with IRAK4 Deficiency. *Ocul Immunol Inflamm* **31**, 874-876 (2023).
21. Barnabei, L., Laplantine, E., Mbongo, W., Rieux-Laucat, F. & Weil, R. NF-kappaB: At the Borders of Autoimmunity and Inflammation. *Front Immunol* **12**, 716469 (2021).
22. Navarro, H.I. *et al.* RelB-deficient autoinflammatory pathology presents as interferonopathy, but in mice is interferon-independent. *J Allergy Clin Immunol* **152**, 1261-1272 (2023).
23. Sharfe, N. *et al.* NFkappaB pathway dysregulation due to reduced RelB expression leads to severe autoimmune disorders and declining immunity. *J Autoimmun* **137**, 102946 (2023).
24. Psarras, A., Wittmann, M. & Vital, E.M. Emerging concepts of type I interferons in SLE pathogenesis and therapy. *Nat Rev Rheumatol* **18**, 575-590 (2022).
25. Liu, Y. *et al.* Activated STING in a vascular and pulmonary syndrome. *N Engl J Med* **371**, 507-518 (2014).
26. Peng, J. *et al.* Clinical Implications of a New DDX58 Pathogenic Variant That Causes Lupus Nephritis due to RIG-I Hyperactivation. *J Am Soc Nephrol* **34**, 258-272 (2023).
27. Psarras, A., Emery, P. & Vital, E.M. Type I interferon-mediated autoimmune diseases: pathogenesis, diagnosis and targeted therapy. *Rheumatology (Oxford)* **56**, 1662-1675 (2017).

28. Hailman, E. *et al.* Lipopolysaccharide (LPS)-binding protein accelerates the binding of LPS to CD14. *J Exp Med* **179**, 269-77 (1994).
29. Wright, S.D., Ramos, R.A., Tobias, P.S., Ulevitch, R.J. & Mathison, J.C. CD14, a receptor for complexes of lipopolysaccharide (LPS) and LPS binding protein. *Science* **249**, 1431-3 (1990).
30. Wright, S.D., Ramos, R.A., Hermanowski-Vosatka, A., Rockwell, P. & Detmers, P.A. Activation of the adhesive capacity of CR3 on neutrophils by endotoxin: dependence on lipopolysaccharide binding protein and CD14. *J Exp Med* **173**, 1281-6 (1991).
31. Shimazu, R. *et al.* MD-2, a molecule that confers lipopolysaccharide responsiveness on Toll-like receptor 4. *J Exp Med* **189**, 1777-82 (1999).
32. Ran, F.A. *et al.* Genome engineering using the CRISPR-Cas9 system. *Nat Protoc* **8**, 2281-2308 (2013).
33. Richard, K. *et al.* A mouse model of human TLR4 D299G/T399I SNPs reveals mechanisms of altered LPS and pathogen responses. *J Exp Med* **218**(2021).
34. He, X.H., Ouyang, D.Y. & Xu, L.H. Injection of Escherichia coli to Induce Sepsis. *Methods Mol Biol* **2321**, 43-51 (2021).
35. Tao, P. *et al.* A dominant autoinflammatory disease caused by non-cleavable variants of RIPK1. *Nature* **577**, 109-114 (2020).
36. Schmid, R. *et al.* Integrative analysis of multimodal mass spectrometry data in MZmine 3. *Nat Biotechnol* **41**, 447-449 (2023).
37. Meng, E.C. *et al.* UCSF ChimeraX: Tools for structure building and analysis. *Protein Sci* **32**, e4792 (2023).
38. Subramanian, A. *et al.* Gene set enrichment analysis: a knowledge-based approach for interpreting genome-wide expression profiles. *Proc Natl Acad Sci U S A* **102**, 15545-50 (2005).
39. Wang, Y. *et al.* Identification of an IL-1 receptor mutation driving autoinflammation directs IL-1-targeted drug design. *Immunity* **56**, 1485-1501 e7 (2023).
40. Hao, Y. *et al.* Integrated analysis of multimodal single-cell data. *Cell* **184**, 3573-3587 e29 (2021).
41. Korsunsky, I. *et al.* Fast, sensitive and accurate integration of single-cell data with Harmony. *Nat Methods* **16**, 1289-1296 (2019).
42. Guilliams, M. *et al.* Dendritic cells, monocytes and macrophages: a unified nomenclature based on ontogeny. *Nat Rev Immunol* **14**, 571-8 (2014).
43. MacParland, S.A. *et al.* Single cell RNA sequencing of human liver reveals distinct intrahepatic macrophage populations. *Nat Commun* **9**, 4383 (2018).
44. Martin, J.C. *et al.* Single-Cell Analysis of Crohn's Disease Lesions Identifies a Pathogenic Cellular Module Associated with Resistance to Anti-TNF Therapy. *Cell* **178**, 1493-1508 e20 (2019).
45. Roquilly, A., Mintern, J.D. & Villadangos, J.A. Spatiotemporal Adaptations of Macrophage and Dendritic Cell Development and Function. *Annu Rev Immunol* **40**, 525-557 (2022).
46. Tang-Huau, T.L. *et al.* Human in vivo-generated monocyte-derived dendritic cells and macrophages cross-present antigens through a vacuolar pathway. *Nat Commun* **9**, 2570 (2018).
47. Villar, J. & Segura, E. Decoding the Heterogeneity of Human Dendritic Cell Subsets. *Trends Immunol* **41**, 1062-1071 (2020).
48. Zhang, L. *et al.* Single-Cell Analyses Inform Mechanisms of Myeloid-Targeted Therapies in Colon Cancer. *Cell* **181**, 442-459 e29 (2020).
49. Zhang, F. *et al.* Defining inflammatory cell states in rheumatoid arthritis joint synovial tissues by integrating single-cell transcriptomics and mass cytometry. *Nat Immunol* **20**, 928-942 (2019).
50. Yao, J. *et al.* Genetic landscape and immune mechanism of monocytes associated with the progression of acute-on-chronic liver failure. *Hepatol Int* **17**, 676-688 (2023).
51. Gulati, G.S. *et al.* Single-cell transcriptional diversity is a hallmark of developmental potential. *Science* **367**, 405-411 (2020).
52. Haghverdi, L., Buettner, F. & Theis, F.J. Diffusion maps for high-dimensional single-cell analysis of differentiation data. *Bioinformatics* **31**, 2989-98 (2015).
53. Street, K. *et al.* Slingshot: cell lineage and pseudotime inference for single-cell transcriptomics. *BMC Genomics* **19**, 477 (2018).
54. Kim, H. *et al.* Development of a Validated Interferon Score Using NanoString Technology. *J Interferon Cytokine Res* **38**, 171-185 (2018).
55. Bravo Gonzalez-Blas, C. *et al.* SCENIC+: single-cell multiomic inference of enhancers and gene regulatory networks. *Nat Methods* **20**, 1355-1367 (2023).

Acknowledgements

We thank the patients, their families, and the unaffected controls for their support during this study.

Funding Statement

Q.Z. discloses support for this work from the National Natural Science Foundation of China [grant number 82225022 and 32321002], National Key Research and Development Program of China [grant number 2024YFC2511002], XPLORER PRIZE from New Cornerstone Science Foundation, Clinical Research Project for the Summit Program of Children's Hospital of Chongqing Medical University [grant number CHCMU-2024-XKDF-1001] and CAMS Innovation Fund for Medical Sciences (CIFMS) [grant number 2024-I2M-3-025]. Z.L. discloses support for this work from the Basic Research Program of Jiangsu [grant number BK20243061]. X.Y. discloses support for this work from the National Natural Science Foundation of China [grant number 82394420, 82471844 and 82394424], the Hundred-Talent Program of Zhejiang University and the Key Technology Breakthrough Program of Ningbo Sci-Tech Innovation YONGJIANG 2035 [grant number 2024Z221]. C.Z. discloses support for the research of this work from the National Natural Science Foundation of China [grant number 82394424]. Y.J. discloses support for the research of this work from the National key research and development project of China [grant number 2021YFC2501302]. Y.W. discloses support for the research of this work from the National Natural Science Foundation of China [grant number 82402088], the Postdoctoral Fellowship Program of CPSF [grant number GZB20230635] and the China Postdoctoral Science Foundation [grant number 2024T170779 and 2024M752825]. S.W. discloses support for the research of this work from the National Natural Science Foundation of China [grant number 82402118]. L.G. discloses support for the research of this work from the Joint Funds of the Zhejiang Provincial Natural Science Foundation of China [grant number LHDMY23H100005].

Author Contributions Statement

Q.Z., Z.L. and X.Y. conceptualized the study, acquired funding, and provided project administration and supervision. Y.F., L.L., S.W., Y.W. and X.S. performed the functional experiments. S.M., X.C., J.W., Y.Y., C.L., J.Z., X.H., J.F. and X.G. analyzed the data. Y.J., L.Z., J.Y., Y.L., M.L., J.X., J.L., Z.K., C.Z., T.H., Z.Liu, L.G., C.C., H.Z., H.Zhong. and L.W. collected and interpreted patients' clinical information. Y.F., L.L., S.M., S.W., Y.W., X.H., C.Z. and Q.Z. wrote the manuscript. All authors contributed to the review and approval of the manuscript.

Competing Interests Statement

The authors declare no competing interests.

Figure Legends

Fig. 1 Clinical findings and identification of the *IRAK2-*Δ*ex2* mutation.

a Pedigrees of eleven unrelated families. Black solid symbols denote affected individuals with a homozygous mutation. All heterozygous carriers are unaffected. A slash indicates a deceased individual. “M” in red indicates the *IRAK2-*Δ*ex2* mutation. **b** Chest computed tomographic (CT) scan of P1 showing dense consolidation with air bronchogram and ground-glass opacities. **c** Chest CT scan of P2 revealing patchy ground-glass opacities and centrilobular nodules. **d-f** Representative renal histopathology images from P3. Eosinophilic deposits in mesangial, subendothelial, and epithelial regions on Masson’s trichrome staining (×400) (**d**). Abundant electron-dense deposits (red arrowheads) in the mesangial areas were detected by electron microscopy (**e**). Immunofluorescence shows diffuse IgG deposition in the mesangial areas and the capillary loops (×400) (**f**). **g** A colonoscopic image of the terminal ileum from P8 revealing mucosal ulcerations (red arrowheads). **h** Representative hematoxylin and eosin-stained image of an ileal biopsy specimen from P8 showing crypt distortion and immune cell infiltration in the lamina propria (×200). **i** A magnetic resonance imaging of P10 showing abnormal signal in the left ilium adjacent to the S2-level sacroiliac joint (circled). Bilateral hip joints exhibited mild effusions with synovial membrane thickening. **j** Distribution of clinical features across twelve patients, grouped by organ system. Each row corresponds to one patient. Blue squares indicate the presence of a symptom; gray squares indicate its absence. The bar graph shows the proportion of symptomatic patients for each feature. GI, gastrointestinal. **k** Sanger sequencing of genomic DNA from twelve patients confirms the homozygous *IRAK2-*Δ*ex2* mutation. The bases flanking the deleted segment (g.10176863 and g.10180996) are referenced to NC_000003.12. **l** Quantitative PCR of *IRAK2* expression in peripheral blood mononuclear cells from P1, P3, P4, P8, P9, P11, and six unaffected controls, using primers located outside (left) or inside (right) exon 2. Bars represent mean of n = 6 ± SEM (biological replicates). Two-sided Student’s t test with Welch’s correction was applied. **m** Transcriptional pattern of *IRAK2* with or without the *IRAK2-*Δ*ex2* mutation.

Fig. 2 Defective NF-κB signaling via Myddosome complex in DIRAK2.

a Structural model of the death domains of IRAK4 (light blue) and IRAK2 (orange; deleted segment in gray) (PDB: 3MOP). Green dotted lines denote predicted intermolecular contacts at the IRAK4-IRAK2 interface. **b** co-immunoprecipitation (co-IP) of whole-cell lysates from HEK293T-*IRAK2* knockout (KO) cells transiently expressing Myc-tagged control empty vector (EV), IRAK2-WT or IRAK2-Δex2, along with equal amounts of EV, IRAK4-Flag or TRAF6-Flag. co-IP was performed using anti-Flag antibody (IP: Flag). **c** Immunoblotting of NF-κB and MAPK signaling in stable HEK293T-TLR4 cells overexpressing control empty vector (EV), IRAK2-WT, or IRAK2-Δex2 after stimulation with 1 µg/mL LPS for indicated times. **d** RNA sequencing analysis of NF-κB pathway in peripheral blood mononuclear cells (PBMCs) from P1, P3, P4, P8, P11, and five unaffected controls. Cells were treated with 1 µg/mL LPS or left unstimulated (UNS) for 12 hours. Each sample was processed in two technical repeats. **e** Cytokine secretion in PBMCs from P3, P4, P11, and six unaffected controls, treated as described in (**d**). Supernatants were analyzed by Cytometric Bead Array. Bars represent mean of n = 6 ± SEM (biological replicates). **f** Expression of IL-6 and IL-10 in 10,000 $CD45^{+}CD66b^{-}$ live PBMCs from P3, P4, and three unaffected controls following LPS stimulation (1 µg/mL, 12 hours), as detected by cytometry by time of flight. Arrowheads indicate monocytes and dendritic cells. **g** Boxplots of NF-κB response scores (single-cell RNA sequencing) in monocytes and plasmacytoid dendritic cells (pDCs) from P3, P4, and three unaffected controls following LPS stimulation (1 µg/mL, 8 hours). Boxplots represent the median and interquartile range, and the whiskers denote minimum and maximum values. The two-sided Wilcoxon rank-sum test was performed.

Fig. 3 Defective NF-κB signaling via Myddosome complex in *Irak2*$^{\Delta ex2/\Delta ex2}$ mice.

a Kaplan-Meier survival curves of *Irak2*$^{\Delta ex2/\Delta ex2}$ and *Irak2*$^{WT/\Delta ex2}$ mice following intraperitoneal (i.p.) injection of LPS (20 mg/kg). The log-rank test was applied. 30-week-old fifth-generation mice were used, with heterozygous littermates as controls. *n* = 10 mice per genotypes (5 females and 5 males). **b, c** Serum cytokine/chemokine levels (**b**) and tissue *Il1b* expressions (**c**) in *Irak2*$^{\Delta ex2/\Delta ex2}$ and *Irak2*$^{WT/WT}$ mice 2 hours after i.p. injection of LPS (10 mg/kg) or PBS. 10-week-old seventh-generation female mice were used, with wild-type (WT) littermates as controls. **d** Hematoxylin and eosin staining of liver tissue centered on the central vein from *Irak2*$^{\Delta ex2/\Delta ex2}$ and *Irak2*$^{WT/WT}$ mice 48 hours after i.p. injection of LPS (1 mg/kg) or PBS. 13-week-old fifth-generation female mice were used, with WT littermates as controls (*n* = 5). **e, f** *E. coli* colony density in peritoneal lavage fluid 4 hours (**e**) and serum Tnf levels 2 hours (**f**) after i.p. injection of *E. coli* (5×10^8 CFU per mouse) in *Irak2*$^{\Delta ex2/\Delta ex2}$ and *Irak2*$^{WT/WT}$ mice. 24-week-old sixth-generation female mice were used, with WT littermates as controls. Two-sided Student's *t* test with Welch's correction was applied. Bars represent mean of *n* = 5 ± SEM (biological replicates). CFU, colony-forming unit. **g** RNA sequencing analysis of NF-κB pathway in bone marrow-derived macrophages (BMDMs) treated with 100 ng/mL LPS or left untreated for 8 hours (*n* = 3, biological replicates). Each sample was processed in two technical repeats. **h** Quantitative PCR of NF-κB-related gene expression in BMDMs treated with 100 ng/mL LPS, 25 ng/mL R848, 50 ng/mL FSL-1, 1 μg/mL Pam_3Cys-Ser-$(Lys)_4$ (PAM3), 2 μM ODN2006, or left unstimulated (UNS) for 8 hours. BMDMs were isolated from 12-week-old fifth-generation female littermate mice. For **b**, **c**, and **h**, two-way ANOVA with Šídák's multiple-comparisons test was applied, and bars represent mean of *n* = 5 ± SEM (biological replicates).

Fig. 4 The *IRAK2*-Δ*ex2* mutation is associated with an increased type I IFN signature.

a Serum IFN-β levels in P1, P3, P4, P8, P9, P11, and six unaffected controls. Boxplots represent the median and interquartile range, and the whiskers denote minimum and maximum values. The two-sided Wilcoxon rank-sum test was performed. **b** Flow cytometric analysis of baseline

phosphorylated IRF3 (p-IRF3) in peripheral blood mononuclear cells (PBMCs) from P1, P8, P11, and three unaffected controls. Geometric mean fluorescence intensities (gMFI; APC-A) are shown in the plots. **c** Gene set enrichment analysis of bulk RNA sequencing from P3, P4, and three unaffected controls following LPS stimulation (1 μg/mL, 12 hours). **d** Uniform manifold approximation and projection (UMAP) of 13 immune cell subsets from P3, P4, and three unaffected controls following LPS stimulation (1 μg/mL, 8 hours). Inflammatory monocytes are circled in red. **e** Differential gene expression analysis of the samples described in (**d**) comparing patients with controls. The two-sided Wilcoxon rank-sum test with Benjamini-Hochberg correction was applied. Dashed line, Log_2 fold change (Log2FC) = 1. **f** Violin plots of IFN-stimulated gene expression in inflammatory monocytes from the samples described in (**d**). Colors represent different individuals. **g** Quantitative PCR (qPCR) of *Ifnb1* expression in bone marrow-derived macrophages (BMDMs) treated with 100 ng/mL LPS, 25 ng/mL R848, 50 ng/mL FSL-1, or left unstimulated (UNS) for 8 hours. BMDMs were isolated from 15-week-old third-generation female littermate mice. Two-way ANOVA with Šídák's multiple-comparisons test was applied. Bars represent mean of n = 5 ± SEM (biological replicates). **h** qPCR of *IFNB1* expression in PMA-differentiated THP-1 cells treated with 10 ng/mL LPS for 0 or 2 hours. Two-way ANOVA with Tukey's multiple-comparisons test was applied. Bars represent mean of n = 5 ± SEM (biological replicates). **i** Principal component analysis of baseline bulk RNA sequencing based on IFN-related genes from DIRAK2 patients (P3, P4, and P8), IRAK4 deficiency (n = 1), IFIH1 mutation (n = 3), DDX58 mutation (n = 5), STING1 mutation (n = 2), genetically undiagnosed SLE (n = 24), and healthy controls (n = 11).

Fig. 5 Evidence supports TRIF-TBK1/IKKε engagement in the elevated type I IFN signature, which is attenuated by JAK inhibition.

a Immunoblotting of *IRAK2*-knockout (KO) THP-1 cells reconstituted with control empty vector (EV), IRAK2-WT, or IRAK2-Δex2 after stimulation with 10 ng/mL LPS for indicated times. **b**

Quantitative PCR (qPCR) of *IFNB1* expression in cells described in (**a**). **c** Immunoblotting of IRF3, IKKε, and TBK1 phosphorylation in reconstituted THP-1 cells stimulated with LPS (10 ng/mL, 2 hours) with or without pretreatment with a TIRAP inhibitor (10 μM, 2 hours) or a TRIF inhibitor (10 μM, 2 hours). **d** qPCR of *IFNB1* expression in cells described in (**c**). LPS++ indicates pretreatment with both inhibitors. **e** Immunoblotting of IRF3 and TBK1 phosphorylation in reconstituted THP-1 cells stimulated with LPS (10 ng/mL, 2 hours) after *TICAM1* (TRIF) knockdown with two independent siRNAs (siRNA#1 and siRNA#2); non-targeting siRNA (siRNA#C) served as control. **f** qPCR of *IFNB1* expression in cells described in (**e**). **g** Immunoblotting of IRF3 phosphorylation in reconstituted THP-1 cells stimulated with LPS (10 ng/mL, 2 hours) with or without pretreatment with a TBK1/IKKε inhibitor (1 μM, 30 minutes) or a TAK1 inhibitor (100 nM, 30 minutes). **h** qPCR of *IFNB1* expression in cells described in (**g**). **i** RNA sequencing of IFN pathway in peripheral blood mononuclear cells (PBMCs) from P4, P11, and three unaffected controls at baseline. P4_Bari and P11_Bari indicate Baricitinib-treated PBMCs (0.5 μM, 12 hours). Freshly isolated PBMCs were sequenced with batch correction. Each sample was processed in two technical repeats. Sample were collected from P4 in April 2023 (P4_1), November 2023 (P4_2), and November 2024 (P4_3 and P4_Bari), and from P11 in May 2025 (P11_1) and June 2025 (P11_2 and P11_Bari). **j** Immunoblotting of the effect of Baricitinib (0.5 μM, 12 hours) on THP-1 cells. **k** qPCR of *IFIT1* and *IFIT3* expression in cells described in (**j**). Two-way ANOVA with Šídák's multiple-comparisons test was applied. Bars represent mean of $n = 5$ ± SEM (biological replicates). For **b**, **d**, **f**, and **h**, two-way ANOVA with Tukey's multiple-comparisons test was applied, and bars represent mean of $n = 5$ ± SEM (biological replicates).

Editor's Summary

Interleukin-1 receptor-associated kinase 2 (IRAK2) is essential for Myddosome complex formation downstream of most Toll-like receptors. Here, the authors show a loss-of-function copy number variant of IRAK2 associated with immunodeficiency, autoimmunity, and autoinflammation, which disrupts IRAK2 interaction with IRAK4 and further downstream Myddosome formation, accompanied by enhanced interferon responses.

Peer Review Information: *Nature Communications* thanks Georgios Sogkas and the other, anonymous, reviewer(s) for their contribution to the peer review of this work. A peer review file is available.

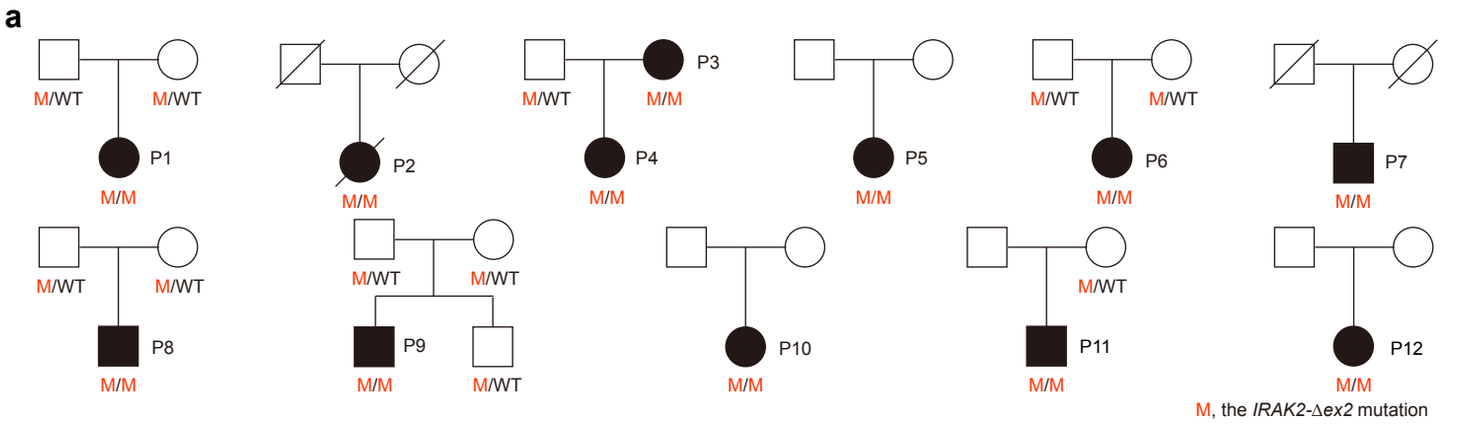
a
M/WT
M/WT
P1
M/M
P2
M/M
M/WT
M/M
P3
P4
M/M
P5
M/M
M/WT
M/WT
P6
M/M
P7
M/M
M/WT
M/WT
P8
M/M
M/WT
M/WT
P9
M/M
M/WT
P10
M/M
M/WT
P11
M/M
P12
M/M
M, the IRAK2-Δex2 mutation

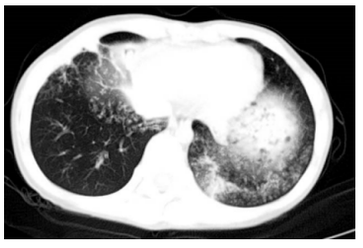
b P1

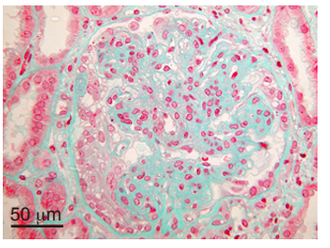
d P3
50 μm

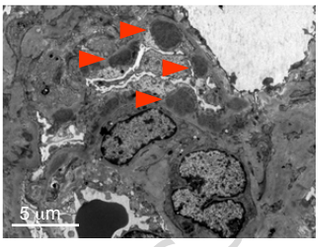
e P3
5 μm

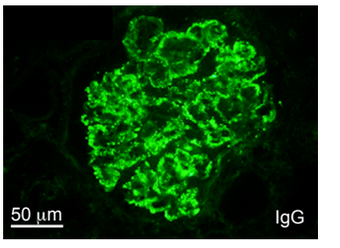
f P3
50 μm
IgG

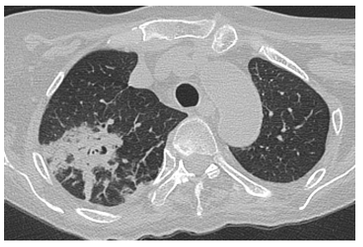
c P2

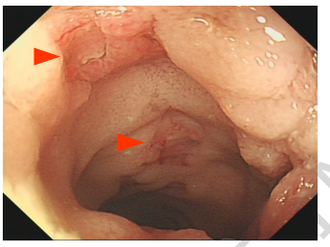
g P8

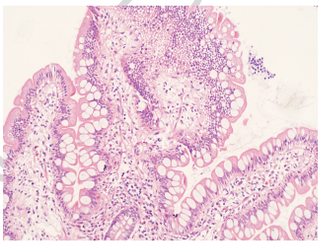
h P8

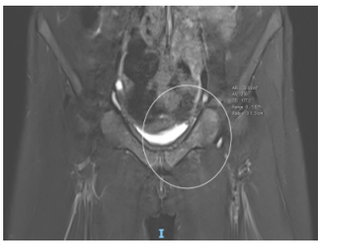
i P10

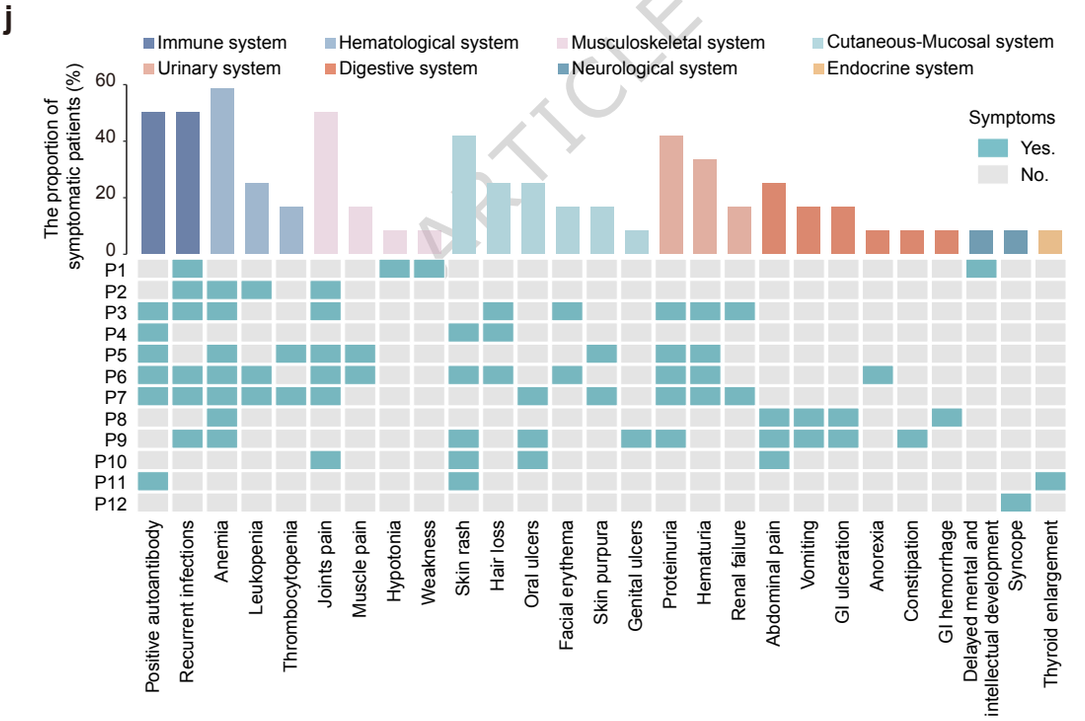
j
Immune system
Hematological system
Musculoskeletal system
Cutaneous-Mucosal system
Urinary system
Digestive system
Neurological system
Endocrine system
The proportion of symptomatic patients (%)
60
40
20
0
Symptoms
Yes.
No.
P1
P2
P3
P4
P5
P6
P7
P8
P9
P10
P11
P12
Positive autoantibody
Recurrent infections
Anemia
Leukopenia
Thrombocytopenia
Joints pain
Muscle pain
Hypotonia
Weakness
Skin rash
Hair loss
Oral ulcers
Facial erythema
Skin purpura
Genital ulcers
Proteinuria
Hematuria
Renal failure
Abdominal pain
Vomiting
GI ulceration
Anorexia
Constipation
GI hemorrhage
Delayed mental and intellectual development
Syncope
Thyroid enlargement

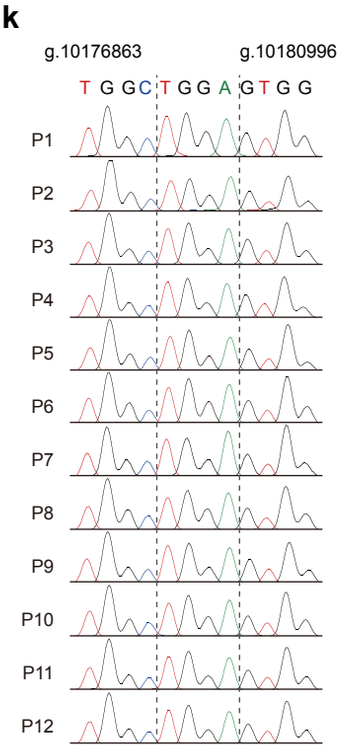
k
g.10176863
g.10180996
T G G C T G G A G T G G
P1
P2
P3
P4
P5
P6
P7
P8
P9
P10
P11
P12

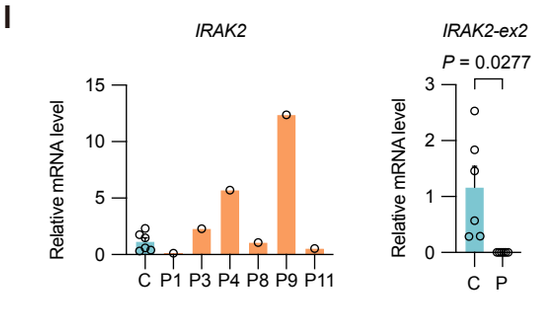
l
IRAK2
Relative mRNA level
15
10
5
0
C P1 P3 P4 P8 P9 P11
IRAK2-ex2
P = 0.0277
Relative mRNA level
3
2
1
0
C P

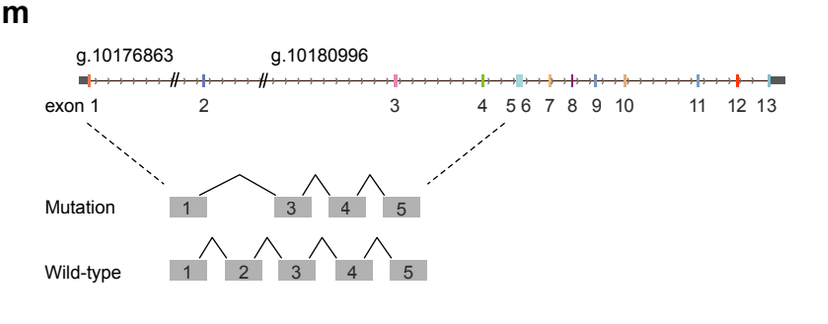
m
g.10176863
g.10180996
exon 1
2
3
4 5 6 7 8 9 10
11 12 13
Mutation
1 3 4 5
Wild-type
1 2 3 4 5

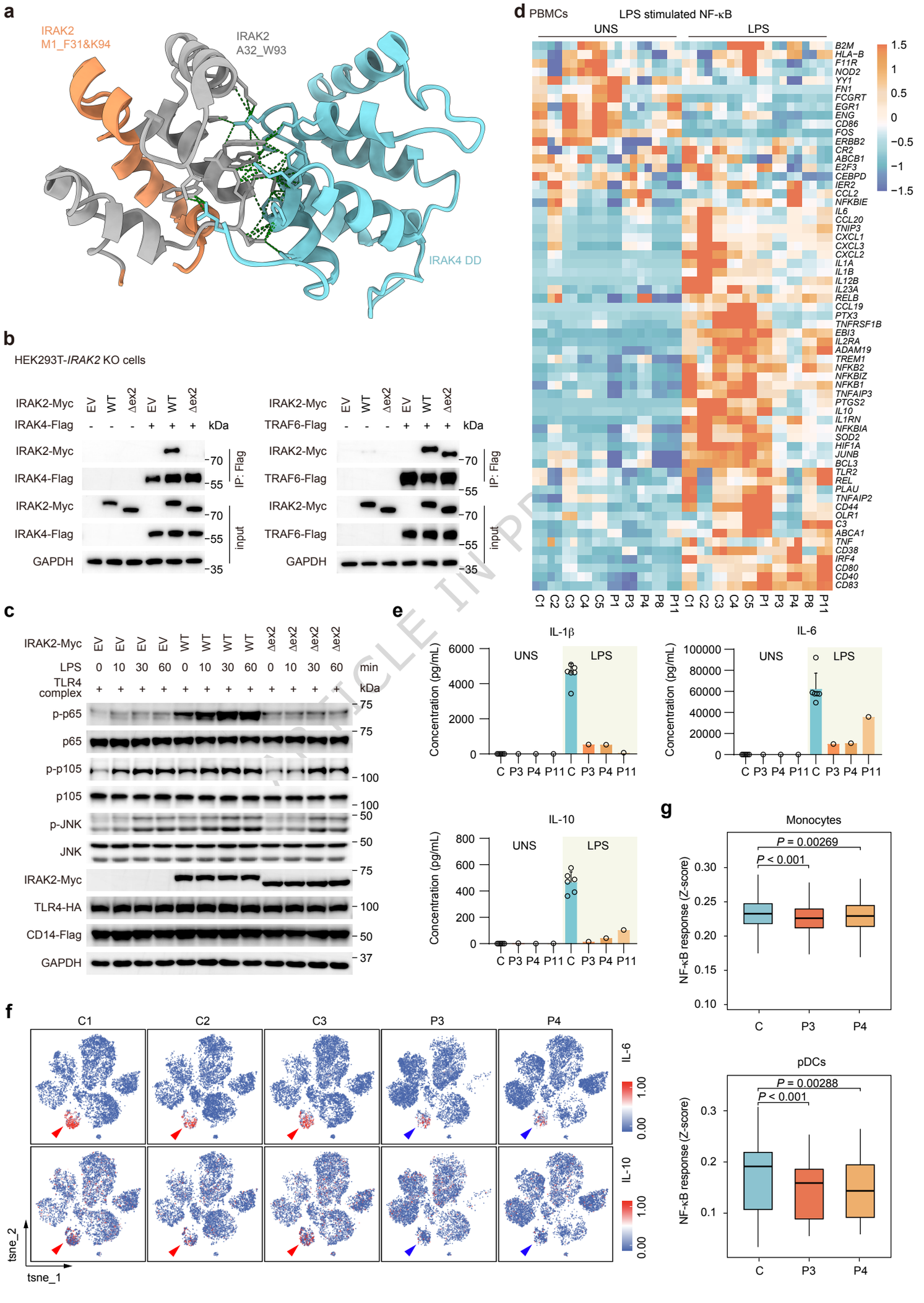

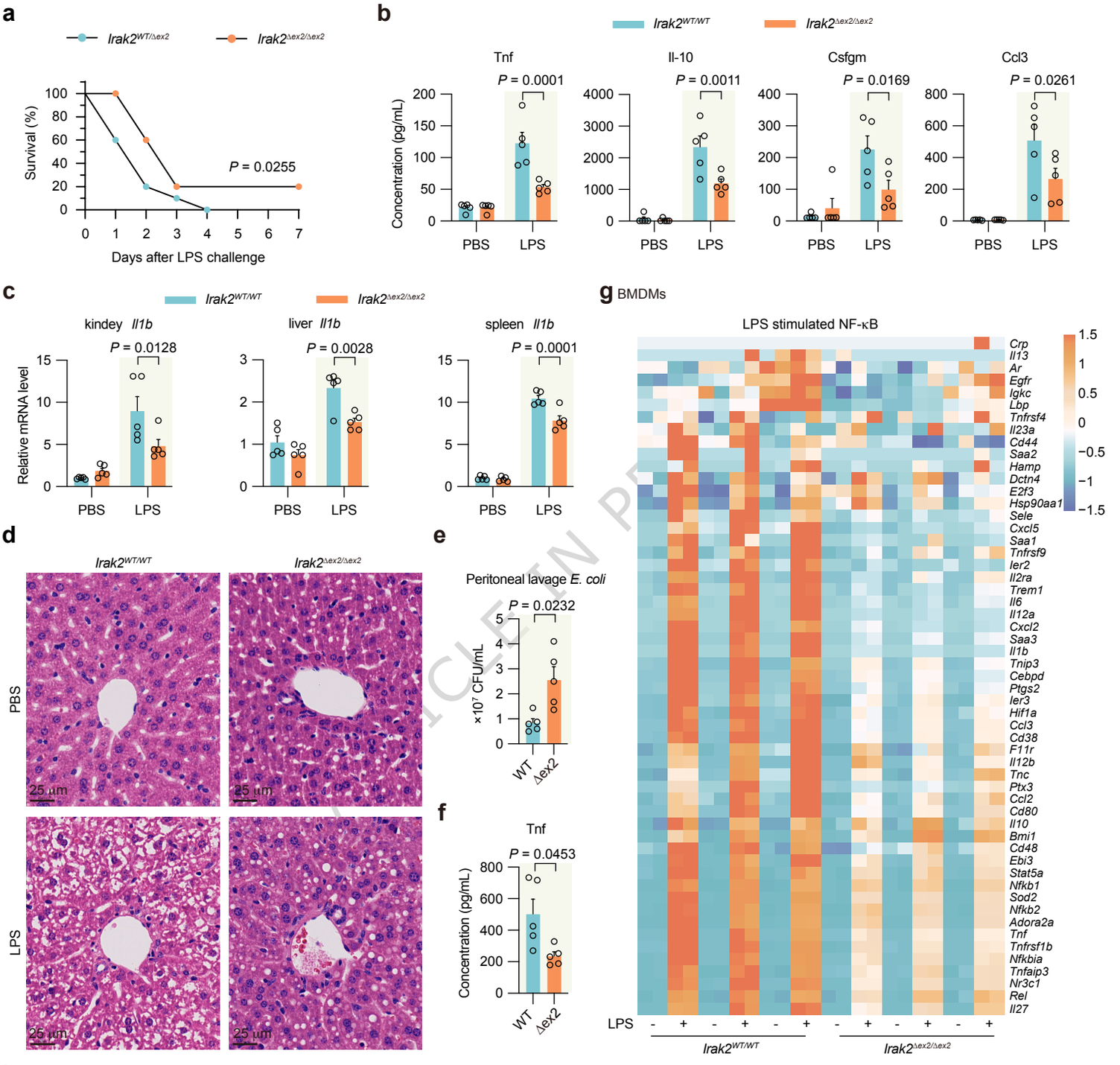
a
Irak2WT/Δex2
Irak2Δex2/Δex2
Survival (%)
P = 0.0255
Days after LPS challenge
b
Irak2WT/WT
Irak2Δex2/Δex2
Tnf
P = 0.0001
Il-10
P = 0.0011
Csfgm
P = 0.0169
Ccl3
P = 0.0261
Concentration (pg/mL)
PBS
LPS
c
kindey Il1b
P = 0.0128
liver Il1b
P = 0.0028
spleen Il1b
P = 0.0001
Relative mRNA level
d
PBS
LPS
25 μm
e
Peritoneal lavage E. coli
P = 0.0232
×10⁷ CFU/mL
WT
Δex2
f
Tnf
P = 0.0453
g BMDMs
LPS stimulated NF-κB
Crp
Il13
Ar
Egfr
Igkc
Lbp
Tnfrsf4
Il23a
Cd44
Saa2
Hamp
Dctn4
E2f3
Hsp90aa1
Sele
Cxcl5
Saa1
Tnfrsf9
Ier2
Il2ra
Trem1
Il6
Il12a
Cxcl2
Saa3
Il1b
Tnip3
Cebpd
Ptgs2
Ier3
Hif1a
Ccl3
Cd38
F11r
Il12b
Tnc
Ptx3
Ccl2
Cd80
Il10
Bmi1
Cd48
Ebi3
Stat5a
Nfkb1
Sod2
Nfkb2
Adora2a
Tnf
Tnfrsf1b
Nfkbia
Tnfaip3
Nr3c1
Rel
Il27
1.5
1
0.5
0
−0.5
−1
−1.5
LPS
h
Il1b
P > 0.9999 P < 0.0001 P < 0.0001 P < 0.0001 P < 0.0001 P = 0.9797
Il6
P > 0.9999 P < 0.0001 P = 0.6465 P < 0.0001 P < 0.0001 P = 0.8197
Relative mRNA level
UNS
LPS
R848
FSL-1
PAM3
ODN2006

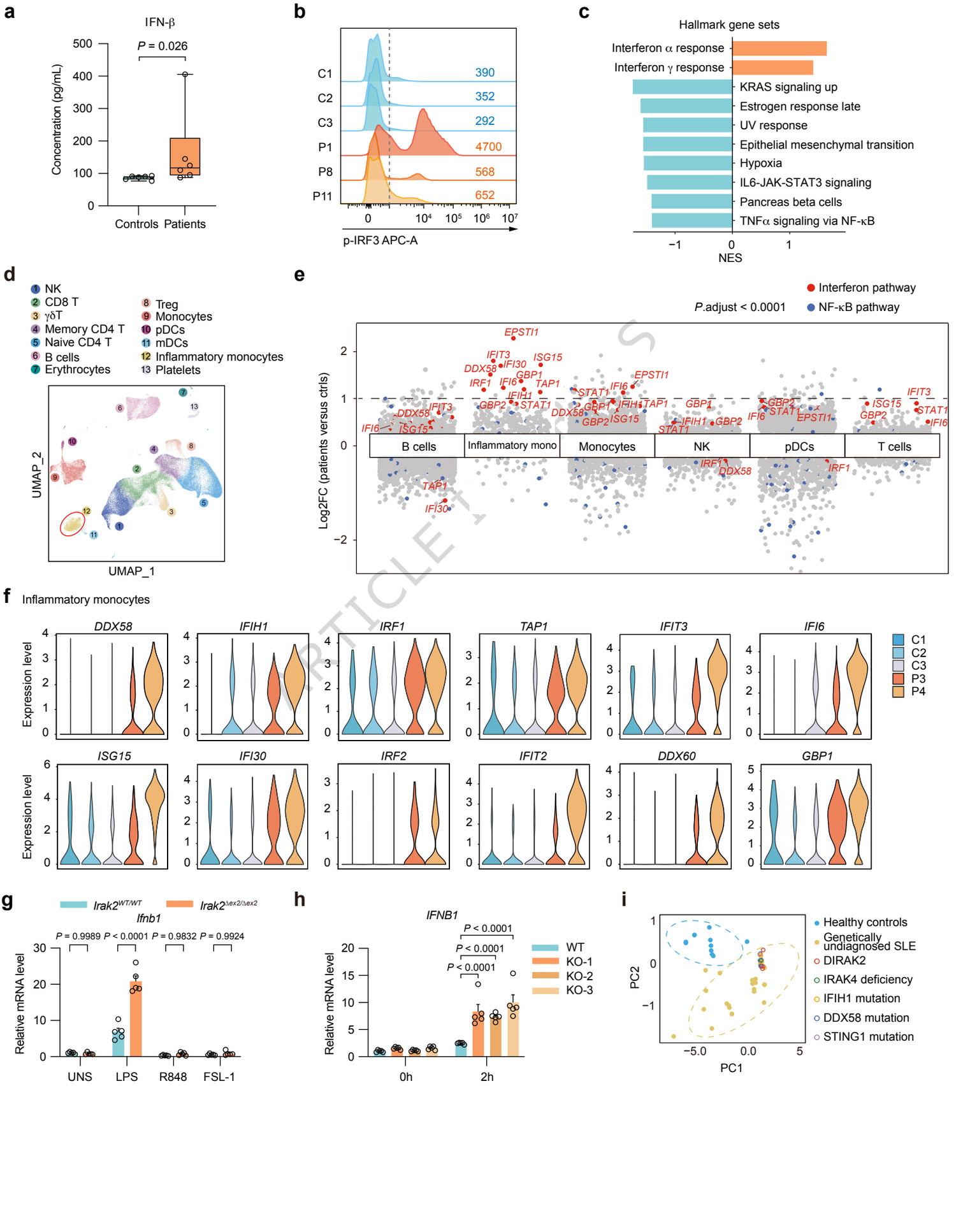
a
IFN-β
P = 0.026
Concentration (pg/mL)
500
400
300
200
100
0
Controls
Patients
b
C1
C2
C3
P1
P8
P11
390
352
292
4700
568
652
0
10⁴
10⁵
10⁶
10⁷
p-IRF3 APC-A
c
Hallmark gene sets
Interferon α response
Interferon γ response
KRAS signaling up
Estrogen response late
UV response
Epithelial mesenchymal transition
Hypoxia
IL6-JAK-STAT3 signaling
Pancreas beta cells
TNFα signaling via NF-κB
−1
0
1
NES
d
1 NK
2 CD8 T
3 γδT
4 Memory CD4 T
5 Naive CD4 T
6 B cells
7 Erythrocytes
8 Treg
9 Monocytes
10 pDCs
11 mDCs
12 Inflammatory monocytes
13 Platelets
UMAP_2
UMAP_1
e
Interferon pathway
NF-κB pathway
P.adjust < 0.0001
Log2FC (patients versus ctrls)
B cells
Inflammatory mono
Monocytes
NK
pDCs
T cells
EPSTI1
IFIT3
ISG15
DDX58
IFI30
GBP1
IRF1
IFI6
TAP1
IFIH1
STAT1
GBP2
IRF1
DDX58
TAP1
IFI30
f
Inflammatory monocytes
DDX58
IFIH1
IRF1
TAP1
IFIT3
IFI6
ISG15
IFI30
IRF2
IFIT2
DDX60
GBP1
Expression level
C1
C2
C3
P3
P4
g
Irak2WT/WT
Irak2Δex2/Δex2
Ifnb1
P = 0.9989
P < 0.0001
P = 0.9832
P = 0.9924
Relative mRNA level
UNS
LPS
R848
FSL-1
h
IFNB1
P < 0.0001
P < 0.0001
P < 0.0001
WT
KO-1
KO-2
KO-3
Relative mRNA level
0h
2h
i
Healthy controls
Genetically undiagnosed SLE
DIRAK2
IRAK4 deficiency
IFIH1 mutation
DDX58 mutation
STING1 mutation
PC2
PC1